Anti-corrosive properties of water-borne acrylic composite coatings using electrochemical methods

By

Leanne Naidoo

Student number: 20406211

Submitted in fulfilment of the requirements of the degree of Master of Applied Sciences in Chemistry in the Faculty of Applied Sciences at the Durban University of Technology

December 2024

DECLARATION

I, **Leanne Naidoo,** declare that the thesis submitted for the degree of Master of Applied Sciences (MAppSci): Chemistry at the Durban University of Technology is the result of my own investigation and has not already been accepted in substance for any degree, and is not being concurrently submitted for any other degree. All the work was done by the author.

Student Name: Mrs L. Naidoo

Signature: …… Date: 16/12/2024

Supervisor Name: Prof K. Bisetty

Signatur …… Date: 16/12/24

Co-Supervisor Name: Dr G. E. Uwaya

Signature: …… Date: 16/12/24

Co-Supervisor Name: Dr T. W. Quadri

Signature: .. Date: 16/12/24

ACKNOWLEDGEMENTS

First and foremost, I wish to express my deepest gratitude to God for granting me the strength and encouragement to persevere through the challenging moments of this journey. I also extend my heartfelt thanks to my beloved Mother Mary for her encouragement and powerful intercession, which have helped me achieve this important milestone in my academic career.

I would like to express my gratitude to Professor K. Bisetty, from the Department of Chemistry at Durban University of Technology (DUT) for his generous guidance and moral support of my research. This thesis is attributed to his immense patience and exceptional guidance and mentorship during my research. Without your assistance, I would not have been able to reach this achievement, and words cannot fully express my appreciation.

I would also like to extend my sincere gratitude to my co-supervisors, Dr. T. W. Quadri from the University of South Africa (UNISA), and Dr. G. E. Uwaya from the Department of Chemistry at Durban University of Technology (DUT), for their assistance in technical matters and their valuable help during the experimental part of the project; your patience, and willingness to assist me, even beyond working hours, have been instrumental in completing my studies.

I would also like to extend my gratitude to Prof. Suvardhan Kanchi and his team from Christ (deemed to university) India, for all his assistance with characterizations of this thesis.

Many thanks to my peers, Dr. Lyndon Naidoo, Khethiwe Mthiyane and Balungile (Rose) Gasa for providing a wonderful research environment. They offered great help and encouragement.

I sincerely appreciate Dr. Reda Fleet from Plascon (part of the Kansai group) for supporting my master's studies and providing access to the necessary raw materials for this project.

A special thank you to my family for their emotional support. To my late dad, Marcus Chetty, whom I lost during my study: you were my inspiration and source of strength. I wish you could be here to see my completion. To my mum, Priscilla, thank you for being my cheerleader, even as we navigated the loss of such an important person in our lives. I would like to dedicate this thesis to Dad, for always believing in me!

To my husband, Shane, thank you for your unwavering support, for standing by me through late nights, and for taking care of our three young children. To my children, Arabella (10), Olivia (5), and Leah (3): I hope to be your inspiration and show you that you can achieve anything your heart desires. Thank you for your love and understanding.

I am deeply grateful to my immediate and extended family for their unwavering love, support, and encouragement throughout this journey. I know I can always count on them for whatever I needed to make this journey possible.

ABSTRACT

This study evaluates the anti-corrosive performance of waterborne acrylic (WBA) nanocomposite coatings on mild steel (MS), incorporating zinc phosphate ($Zn_3(PO_4)_2$), graphene oxide (GO), and polyvinylpyrrolidone (PVP). The WBA composites were synthesized and characterized using Fourier-transform infrared spectroscopy (FTIR), X-ray diffraction (XRD), and field emission scanning electron microscopy (FESEM). FTIR analysis confirmed the successful formation of polymer nanocomposites, revealing the presence of functional groups associated with the incorporated nanomaterials. XRD, distinguished between crystalline and amorphous structures within the coatings. FESEM, coupled with energy-dispersive spectroscopy (EDS), offered detailed morphological and elemental analyses, confirming the uniform distribution of nanomaterials within the polymer matrix. The corrosion resistance of the coated MS surfaces was evaluated in a 5% sodium chloride (NaCl) aqueous solution using electrochemical techniques such as potentiodynamic polarization (PDP), linear polarization resistance (LPR), and electrochemical impedance spectroscopy (EIS). Additionally, environmental durability was assessed through salt spray tests and QUV® accelerated weathering, simulating harsh conditions to evaluate the longevity and performance of the coatings.

Among the formulations, WBA-$Zn_3(PO_4)_2$ demonstrated the most effective corrosion resistance, surpassing other formulations. EIS measurements demonstrated a charge transfer resistance (R_{ct}) of 63.9 kΩ·cm² and an inhibition efficiency (η_{EIS}) of 93.76%. The open circuit potential (OCP) was measured at 0.78 V This performance was attributed to the strong passivation effect of the phosphate ions, which minimized the anodic and cathodic reactions. PDP analysis showed the lowest corrosion current density (i_{corr}) of 2 µA/cm² and a corrosion potential (E_{corr}) of -668 mV, confirming strong passivation by phosphate ions. WBA-GO showed moderate protection due to its barrier properties, but its effectiveness was slightly lower due to defects in the graphene oxide (GO) layer. EIS measurements demonstrated a charge transfer resistance of Rct of 14.5 kΩ·cm² and ηEIS of 69.93%. The icorr was recorded at 8 µA/cm² with an Ecorr of -504 mV.

Coatings containing PVP, such as WBA-PVP, WBA-GO/PVP, and WBA-$Zn_3(PO_4)_2$/PVP, exhibited significantly lower Rct values ranging from 1.42 to 8.3 kΩ·cm², with negative inhibition efficiencies between -116.92% and -207.04%. These negative values suggest that PVP-containing coatings disrupted passivation, leading to increased corrosion rates. The hydrophilic nature of PVP may have contributed to these adverse effects, compromising the coatings' barrier properties.

Environmental exposure tests further confirmed WBA-$Zn_3(PO_4)_2$ superior durability, with minimal discolouration (ΔE = 9) and strong adhesion (4B rating) after 48 hours of salt spray exposure. WBA-GO (ΔE = 15) and WBA-PVP (ΔE = 22) showed greater degradation. Phosphate ions in WBA-$Zn_3(PO_4)_2$ minimized anodic and cathodic reactions, enhancing corrosion resistance. Optical profilometry provided 2D and 3D topographies of the bare metal surface, displaying the presence of iron peaks and confirming the corrosion susceptibility and the elemental composition of mild steel

Results indicate that the WBA-$Zn_3(PO_4)_2$, emerged as the most effective anti-corrosive coating, offering superior corrosion resistance, minimal blistering, and excellent adhesion due to its strong passivation and barrier properties. While, WBA-GO displayed reasonable protective properties but were slightly less effective than WBA-$Zn_3(PO_4)_2$. The weakest performers were WBA-PVP and WBA-GO/PVP, which struggled with limited resistance and adhesion issues.

These findings suggest that optimally formulated water-borne acrylic nanocomposites are eco-friendly alternatives with low VOC content and can offer a sustainable solution for corrosion protection in harsh environments.

TABLE OF CONTENTS

LIST OF FIGURES

LIST OF TABLES

LIST OF ACRONYMS AND SYMBOLS

0D	Zero-dimensional
1D	One-dimensional
2D	Two-dimensional
3D	Three-dimensional
AC	Alternating current
βa	Tafel slope
βc	Cathodic Tafel slope
ΔE	Change in colour
CE	Counter electrode
CPE	Constant phase element
DFT	Dry film thickness
Dlc	Double-layer capacitance
E_{corr}	Corrosion potential
EDX	Energy dispersive X-ray spectroscopy
EIS	Electrochemical impedance spectroscopy
Fe	Iron
FESEM	Field emission scanning electron microscopy
FTIR	Fourier transform infrared spectroscopy
GO	Graphene oxide
i_{corr}	Corrosion current density
ISO	International Organization for Standardization
LPR	Linear polarization resistance
MS	Mild steel
NaCl	Sodium chloride
OCP	Open circuit potential
PDP	Potentiodynamic polarization
PVP	Polyvinylpyrrolidone
R_{ct}	Charge transfer resistance
RE	Reference electrode
GO	Reduced graphene oxide
R_s	Solution resistance

RMS	root mean square
SS	Salt spray
SEM	Scanning electron microscopy
TEM	Transmission electron microscopy
TGIC	Triglycidyl isocyanurate
VOC	Volatile organic content
W	Warburg element
WE	Working electrode
WFT	Wet film thickness
XRD	X-ray diffraction
$Zn_3(PO_4)_2$	Zinc phosphate
$Zn_2Fe(PO_4)_2 \cdot xH_2O$	Zinc-iron phosphate hydrate
ZnO	Zinc oxide

LIST OF PUBLICATIONS & CONFERENCES

Publication (Submitted)

Leanne Naidoo, Gloria Ebube Uwaya, Taiwo W. Quadri, Suvardhan Kanchi, and Krishna Bisetty*, Corrosion Resistance of Water-Borne Acrylic (WBA) Composites for Mild steel Protection in 3.5% NaCl solution. *J. Coat. Technol. Res (Submitted April 2025).*

Conference

L. Naidoo, “Anti-corrosive properties of water-borne acrylic composite coatings using electrochemical methods”, 7th International Symposium on Electrochemistry from 13-16 April 2025 at the Southern Sun

CHAPTER 1 - INTRODUCTION

This chapter presents a brief overview of the study, with a particular emphasis on investigating anti-corrosive material activities in waterborne acrylic coatings via electrochemical analyses. The aim and objectives of this work are also presented followed by a brief outline of this thesis.

1.1) Background and Problem Statement

Water-borne acrylic coatings are widely employed in industry, to reduce corrosion, and extend the lifetime of the applied surfaces (Akpan *et al.* 2022; Wang *et al.* 2022). These coatings are formulated by dispersing acrylic polymers, various additives and anti-corrosive materials into water, making them environmentally friendly, with a lower volatile organic content (VOC) (Gao *et al.* 2021b). In addition, they serve as the most common, cost-effective, and efficient method for anti-corrosive coating development (Pourhashem *et al.* 2020).

Corrosion is a natural chemical process, known to cause deterioration, of solid metallic structures, via electrochemical reactions, resulting from the potential difference, between the metal and associated electrolyte (Shumaila *et al.* 2022). These corrosive reactions, change the microstructure of the metal, which results in the loss of its elasticity, mechanical and tensile strength, forming flaky and brittle units (Gao *et al.* 2021a). The consequences of corrosion, are irreversible and unavoidable processes, that lead to the loss of billions of dollars in the chemical, construction, transport and oil industries (Mishra *et al.* 2020). Corrosion can be hindered through various prevention strategies, which include the use of corrosion inhibitors (chemical barriers), anti-corrosive coatings (physical barriers), design modifications and anodic/cathodic protection (Yao *et al.* 2022) . Among the various methodologies, anti-corrosive coatings have emerged as the most common, cost-effective, and efficient method, for reducing corrosion and extending the lifetime of the substrates, by forming a physical barrier between the harmful environment and the metal surface (Pourhashem *et al.* 2020).

However, such coatings have challenges that persist, particularly in marine systems, as saline solutions, tend to penetrate and deteriorate metallic surfaces. Therefore, chemical additives are used as corrosion inhibitors, in anti-corrosive coatings, at low concentrations, to prevent the progression of corrosion (Sam John 2012; Yao *et al.* 2022).

Traditional anti-corrosion coatings depend on solvent-based systems containing toxic corrosive inhibitors, and pigments, such as lead or hexavalent chromium compounds. But, with increasing environmental regulations and the demand for greener technologies, there is a shift toward waterborne coatings that have lower volatile organic compounds (VOCs) (Yao *et al.* 2022). Water offers two main advantages as a solvent: it is non-toxic and non-flammable, and it eliminates the need for costly cleaning solvents, as brushes and spray guns can be cleaned with water. Waterborne acrylic coatings have become a cost-effective and eco-friendly alternative for corrosion protection due to their low VOC content and ease of application (Pourhashem *et al.* 2020). However, current water-based acrylic coatings, have limitations, particularly in marine environments, as conventional waterborne coatings are susceptible to degradation under harsh conditions. Prolonged exposure to saline environments can lead to water-induced blistering, cracking, and eventual failure of the coating (Ecco *et al.* 2016; Ress, Martin and Bastidas 2021).

Therefore, the development of such systems has prompted the incorporation of nanomaterials, zinc phosphate $Zn_3(PO_4)_2$, polyvinylpyrrolidone (PVP) and graphene oxide (GO), into water-borne coatings, to offer barrier properties, to prevent the percolation of corrosive ions (John, Kuruvilla and Joseph 2013; Necolau and Pandele 2020; Yang *et al.* 2022).

These nanomaterials have exhibited promising results, owing to their physical, mechanical and anti-corrosive properties resulting from their ability to reduce pore spaces and create a tortuous pathway for aggressive aqueous ions (Pourhashem *et al.* 2020).

Researchers have reported that zinc phosphate forms a passive layer on metal surfaces, inhibiting both anodic and cathodic reactions (Chimenti 2019), whereas, graphene oxide reduces ion permeability by creating tortuous pathways (Al Juhaiman,

Mustafa and Mekhamer 2012), while PVP helps form a uniform, adherent film that minimizes defects and reduces the rate of corrosion (Zheng Liu 2022).

In this work, the anti-corrosive properties of synthesized nanocomposite coatings were investigated on mild steel in a saline medium using electrochemical impedance spectroscopy (EIS) and potentiodynamic polarization (PDP) techniques coupled with salt spray and ultraviolet exposure tests. Analytical tools such as Fourier transform infrared (FTIR), X-ray diffraction (XRD), field emission scanning electron microscopy (FESEM), energy dispersive X-Ray spectroscopy (EDX) and optical profilometry were used to characterize the synthesized nanocomposite coatings.

1.2) Aim and objectives

Aim

To develop an effective and efficient anti-corrosive coating formulation based on water-borne acrylic composites to remedy problems associated with the corrosion of mild steel in a saline medium.

Objectives

The objectives of this thesis are:

- To synthesise water-borne acrylic composites comprising of commercially available zinc phosphate ($Zn_3(PO_4)_2$), polyvinylpyrrolidone (PVP) and graphene oxide (GO).
- To characterize $Zn_3(PO_4)_2$, PVP, GO and the water-borne acrylic composites using FTIR, XRD, FESEM, EDX and Optical Profilometry.
- To evaluate the corrosion protection properties of the water-borne acrylic composites using electrochemical impedance spectroscopy (EIS) and potentiodynamic polarization (PDP) as electrochemical methods.
- To evaluate the effectiveness of the anti-corrosive coatings, using a salt spray chamber under accelerated weathering conditions.

1.3) Overview of the thesis

This thesis is divided into six chapters. The chapters are divided as follows:

Chapter 1

This chapter presents an overview of corrosion, with a focus on the role of anti-corrosive nanomaterials in water-borne acrylic composites. It includes the aims and objectives of the study, as well as a brief outline of the thesis structure.

Chapter 2

Presents a literature review of anti-corrosive nanomaterials and an insightful understanding of previous anti-corrosion materials used to reduce the rate of corrosion. Additionally, electrochemical applications in the detection of corrosion are also discussed.

Chapter 3

Outlines the theoretical principles and provide a brief overview of the analytical instruments used, followed by the theoretical principles associated with the calculations.

Chapter 4

Describes the materials and methods used for the experimental work used in this study.

Chapter 5

The results obtained from the experimental studies are based on the design and characterization of the electrochemical techniques and the effects of the anti-corrosive nanomaterial in water-borne acrylic composites

Chapter 6

Provides a summary of the conclusions and recommendations of this work.

CHAPTER 2 - LITERATURE REVIEW

This chapter presents a literature review of anti-corrosive nanomaterials used to protect mild steel from corrosion by understanding, the principles of corrosion, the environmental factors, and the conditions under which corrosion occurs. Additionally, the composition and manufacturing processes of anti-corrosive coatings are discussed here.

2.1) Principles of corrosion

2.1.1) Composition of mild steel

Mild steel is the most common type of steel, accounting for more than 90% of all steel produced worldwide. Steel products are described as mild, medium or high according to the percentage of carbon to iron they contain. Mild steel is an iron alloy that is inherently heterogeneous and impure and contains less than 0.25% carbon. Therefore, mild steel is an affordable material that is versatile and used in a wide variety of applications such as the construction, chemical, transport and oil industries (Callister Jr and Rethwisch 2020).

2.1.2) Consequences of corrosion

The economic impact of corrosion is substantial and is coupled with considerable environmental and health hazards. One-third of annual steel loss is directly attributed to corrosion, which contributes to incidents such as pipeline leaks, explosions, and structural collapses, resulting in severe injuries and preventable fatalities (Pikaar *et al.* 2014; Mishra *et al.* 2020). The National Association of Corrosion Engineers reported an annual global corrosion cost of approximately US $2.5 trillion, with South Africa alone incurring an estimated R130 billion per year (Varney *et al.* 2016; Mishra *et al.* 2020).

2.1.3) Mechanism of corrosion in Saline Environments

Corrosion in saline environments is an electrochemical process accelerated by chloride ions and the high conductivity of saltwater, leading to more rapid metal degradation (**Figure 2.1**). The process occurs in the following steps:

Step 1. Formation of Electrochemical Cells

Iron corrosion in saline environments occurs through the formation of small electrochemical cells on the metal surface. These cells consist of:

- Anodic regions, where iron (Fe) oxidizes, releasing electrons.
- Cathodic regions, where oxygen (O_2) is reduced using the electrons released at the anode.

Step 2. Anodic Reaction (Iron Oxidation)

At anodic sites, iron atoms lose electrons and dissolve as ferrous ions:

$$Fe \rightarrow Fe^{2+} + 2e^-$$

In the presence of excess oxygen, ferrous ions ($^{Fe2+}$) can further oxidize to ferric ions (Fe^{3+}):

$$Fe^{2+} \rightarrow Fe^{3+} + e^-$$

Step 3. Cathodic Reaction (Oxygen Reduction)

At the cathodic sites, dissolved oxygen from the environment reacts with water and electrons to form hydroxide ions:

$$½O_2 + H_2O + 2e^- \rightarrow 2OH$$

Step 4. Role of Chloride Ions (Cl^-)

Chloride ions (Cl^-) in saline water accelerate corrosion by:

- Increasing the conductivity of the electrolyte, allowing faster electron flow.
- Destabilizing the passive oxide layer on iron, exposing more metal to corrosion.

- Forming soluble complexes with iron ions, preventing the formation of protective corrosion products.

Step 5. Formation of Corrosion Products

The reaction between iron ions (Fe^{2+}, Fe^{3+}) and hydroxide ions (OH^-) results in the formation of iron hydroxides:

$$Fe^{2+} + 2OH^- \rightarrow Fe(OH)_2$$

$$Fe^{3+} + 3OH^- \rightarrow Fe(OH)_3$$

These hydroxides further react with oxygen and water to form hydrated iron oxides (rust), which appear as a reddish-brown layer on the metal surface:

$$Fe(OH)_3 \rightarrow Fe_2O_3 \cdot xH_2O \text{ (Rust)}$$

6. Continuous Corrosion Cycle

- Rust is porous and does not provide a protective barrier, allowing continued exposure to oxygen, water, and chloride ions.
- As a result, the corrosion process persists, leading to structural weakening of the metal over time.

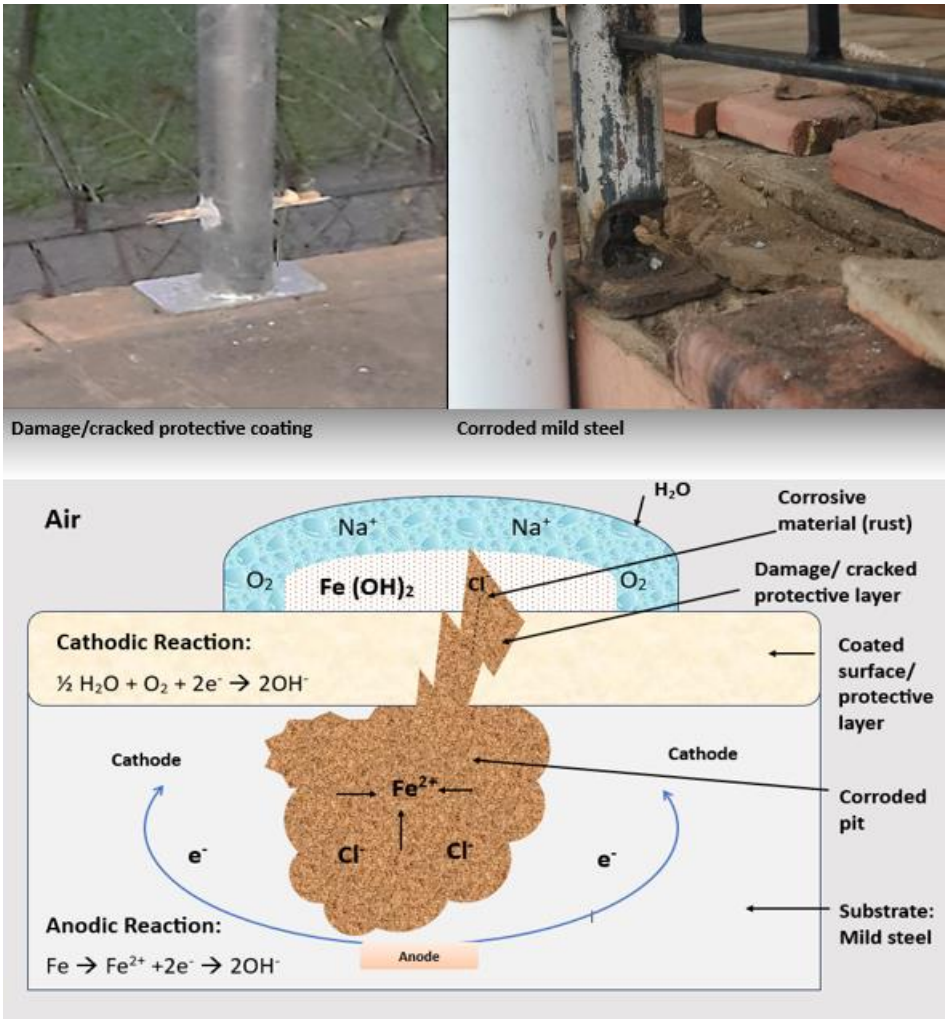

Figure 2:1. Electrochemical corrosion process of mild steel in an electrolyte.

2.1.4) Conditions of corrosion

For corrosion to occur, certain conditions must be present. The key factors that influence corrosion can be summarized as follows (Boumhara *et al.* 2018):

- **Metal**: This includes the composition, atomic structure, microscopic and macroscopic heterogeneities or imperfections, as well as the presence of stress (tensile, compressive, or cyclic).
- **Environment**: The chemical properties, concentrations of reactive species and harmful impurities, pressure, and temperature all play significant roles in the corrosion processes.

- **Metal/environment interface**: This refers to the kinetics of metal oxidation and dissolution, the reduction of species in solution, the nature and distribution of corrosion products, the growth and dissolution of the protective film.

2.1.5) Forms of corrosive degradation

Corrosion caused by rust is usually red, brown or black in colour and occurs in various forms. The common types of corrosion that usually occur on metals are listed below:

- Filiform corrosion
- Galvanic corrosion
- Uniform corrosion
- Microbial Corrosion
- Pitting corrosion

Filiform corrosion

Corrosion manifests in various forms, each influenced by the specific type of metal degradation and the surrounding corrosive environment (Mishra *et a*l., 2020). When moisture infiltrates a coated surface, it leads to tunnel formation beneath the coating (**Figure 2.2**) (Mishra *et al.* 2020).

Figure 2:2. Formation of filiform corrosion.

Galvanic corrosion

Arises when two dissimilar metals, which have different electrochemical potentials, are physically connected and exposed to a conductive electrolyte. For example, the degradation of mild steel fasteners (screws) in contact with aluminium, in a corrosive

environment demonstrates this process. (**Figure 2.3**) (Kelly 2017; Shumaila *et al.* 2022).

Figure 2:3. Galvanic corrosion.

Uniform corrosion

Occurs as the most common type of corrosion, that is evenly distributed across the metal surface, resulting in predictable degradation. This type of corrosion, significantly, affects material performance, as progress of degradation has no control. **(Figure 2.4)** (Mobin and Shabnam 2010).

Figure 2:4. Uniform corrosion.

Microbial corrosion

This phenomenon occurs due to the activity of microbes, such as viruses or bacteria, which often cause pitting. This type of corrosion can be controlled using biocides or conventional corrosion prevention techniques (**Figure 2.5**) (Singh 2020).

Figure 2:5. Microbial corrosion.

Pitting corrosion

It is one of the most hazardous forms of corrosion, because its highly localized and has an unpredictable nature, which makes detection difficult. It forms small pits or holes that grow over time, potentially leading to structural failure. For example, a water droplet on steel, initiates pitting at the site of the droplet. (**Figure 2.6**) (Vignal *et al.* 2007).

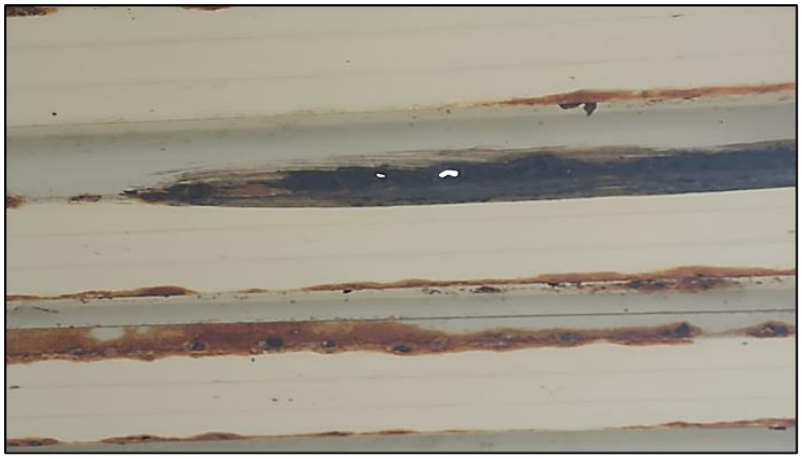

Figure 2:6. Pitting corrosion.

2.1.6) Corrosive environment

A corrosive environment refers to the surrounding conditions that can lead to metal degradation. ISO 12944, provides guidelines for selecting protective coatings based on the corrosive environment and atmospheric conditions, in which the product is located. It categorizes environments ranging from rural areas, with minimal corrosive exposure to harsh marine environments, where airborne salts are prevalent.

Corrosion risk in indoor areas is generally lower due to fewer atmospheric pollutants. However, poor ventilation or high humidity can lead to condensation, increasing the risk of corrosion. ISO 9223:2017 defines corrosion levels, classifying environments from C1 (very low corrosion, typical of climate-controlled indoor spaces) to C5 (very high corrosion, such as coastal refineries) **(Appendix 1)**.

In addition, ISO 12944 has introduced the CX **(Appendix 1)** and IM categories **(Appendix 2)**, which addresses, more detailed corrosion classification for underwater and underground structures.

2.1.7) Corrosion protection strategies

Corrosion prevention, aims to eliminate or minimize conditions, that lead to corrosion, through various strategies to protect materials, especially metals, from degradation. These methods include optimized design, electrochemical protection, environmental modification, material selection, and corrosion inhibitors through protective coatings (Revie and Uhlig 2008).

Material selection is fundamental for corrosion resistance, as different materials offer varying durability and costs. Stainless steel, for example, has a high chromium content, that enhances resistance to corrosion, but, is a more expensive alternative to mild steel. Galvanizing mild steel with zinc provides a cost-effective corrosion barrier, but it releases toxic fumes when welded, limiting its use in some applications (Mobin and Shabnam 2010).

Electrochemical protection uses an effective strategy, offering cathodic protection (CP) that protects the metal into the cathode of an electrochemical cell, protecting it from corrosion. This approach includes the following steps (Bierwagen 1998).

- Sacrificial anode protection which uses a more reactive metal, such as aluminum or zinc, to corrode in place of the protected metal.
- Impressed current protection involves applying a low-voltage current with insoluble anodes like silver, which, although effective, can be costly.

Therefore, the most cost-effective method for preventing corrosion, is the use of anti-corrosive coatings. Anti-corrosive coatings are designed with small dosages of

corrosion inhibitors, to reduce or stop both cathodic and anodic reactions, by lowering the diffusion rate of reactants, or increasing the electrical resistance of the metal surface, through the adsorption of ions/molecules on the surface of the metal. Forming an impenetrable barrier, that protects, the substrate from the aggressive environment (Saji 2012; Barroso 2014; Sillanpää and Shestakova 2017).

These anti-corrosive coatings are composed of binders, solvents, pigments and additives. The binder forms an adhesive film over the metal substrate, enhancing properties such as flexibility, hardness, and UV resistance. Common binder types acrylic, alkyd, polyurethanes, and epoxies, which are tailored for specific applications.

Traditional, anti-corrosive coatings, such as epoxy and acrylic coatings, are cost-effective but often release VOC's and contain carcinogenic pigments such as lead and hexavalent chromium compounds. Eco-friendly waterborne acrylic coatings are emerging as a sustainable solution in protecting the environment, whilst emerging nanomaterials offer unique properties, to these coatings, further increasing the protection of the material (metal) by slowing the corrosive diffusion element and enhancing durability (Wan *et al.* 2021; Liu *et al.* 2022; Wang *et al.* 2022).

2.1.8) Protection mechanism

There are three major types of coatings, for the protection mechanism of steel. Methods include corrosion inhibitor through a surface coating, cathodic protection by electrochemically active coatings and ion deprivation coatings, forms a barrier that disrupts the ionic pathways needed for corrosion reactions (**Figure 2.7**) (Revie and Uhlig 2008).

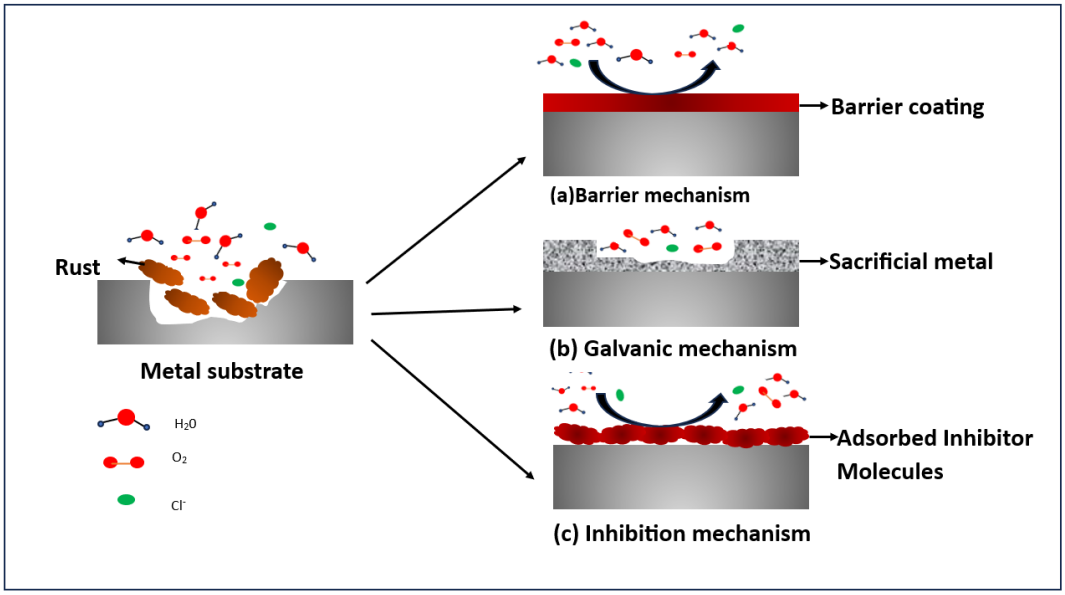

Figure 2:7. Schematic illustration of the **(A)** barrier; **(B)** galvanic; and **(C)** inhibitive mechanisms.

Barrier coatings, **(Figure 2.7a),** physically protects the metal surface, by preventing contact between the metal and a corrosive medium. These coatings mainly react by impeding ionic conduction and increasing electrical resistance or by reducing anodic and cathodic reactions. This method limits the penetration of water and oxygen that can attack the metal surface. However, water permeation remains a critical factor, as it weakens the coating adhesion and promotes blistering on the coated substrate (Yao *et al.* 2022; Chen *et al.* 2023).

Galvanic Mechanism (**Figure 2.7b)** are electrochemically active coatings, that protect the metals through sacrificial corrosion or conductive polymers. Sacrificial coatings, contain metals like zinc or magnesium, corrode preferentially, providing cathodic protection. Conductive polymers modify corrosion potential and form a diffusion barrier, further preventing metal degradation. (Ress, Martin and Bastidas 2021).

The inhibition mechanism **(Figure 2.7c)** functions by integrating corrosion inhibitors into the coating's binders. These inhibitors, serve as additives or pigments, promoting surface passivation by forming a protective layer on the substrate. This layer acts as a barrier, preventing the penetration of aggressive species. For example, zinc oxide and calcium nitrite function as mixed inhibitors, suppressing both anodic and cathodic corrosion reactions. (Camila and Alexandre 2014; Umoren and Solomon 2014; Lei *et al.* 2020; Mishra *et al.* 2020).

2.1.9) The composition of anti- corrosive coatings

Acrylic waterborne anti-corrosive coatings consist of four main components: pigments and extenders, binders, solvents, and additives, as shown in **Figure 2.8**.

Organic polymers known as binders/ resin make up a majority composition of the coating composition. Binders are categorized as either Water-borne or solvent-based and can be classified into acrylics, polyurethanes, or alkyds. The resin is responsible for forming a robust, protective film that ensures adhesion, hardness, and chemical resistance are critical for corrosion prevention (Lyon, Bingham and Mills 2017).

Solvents are incorporated into coating formulations to lower the viscosity, ensuring smooth application. In Water-borne systems, water serves as the primary solvent, offering environmental advantages by reducing VOC emissions. (Xia *et al.* 2023).

Additives, the most expensive part of the formulation, make up a small percentage of the formula, enhancing properties such as drying time, stability, and anti-corrosive resistance to optimize performance under challenging conditions (Low *et al.* 2023).

Pigments, which also often constitute minimally relative to the total formulation, provide colour and opacity, and extenders are included to aid in the coating hardness when cured, but does not contribute to colour (Maile, Pfaff and Reynders 2005).

Pigments and extenders are supplied as powders with large particle sizes; therefore, it is necessary to reduce and stabilize the particles size of the pigment to prevent the formation re-agglomeration. This process, known as “pigment dispersion,” involves wetting, de-aggregation, and stabilizing particles to prevent re-aggregation (Maile, Pfaff and Reynders 2005). A reduction in particle size contributes to a dry film that is of the correct colour, smooth, glossy and opaque.

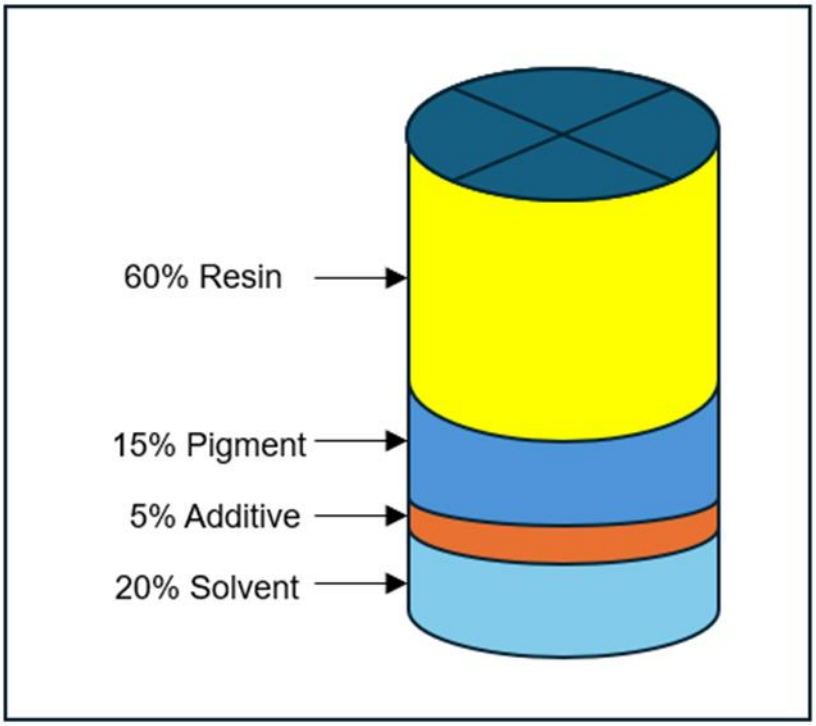

Figure 2:8. Composition of Water-borne acrylic anti-corrosive coatings.

2.1.10) Pigment dispersion

Resins and solvents are blended to form the “vehicle” for the pigment dispersion. These concentrated pigment dispersions, known as the “mill base”, are blends of resin, solvents, and additives. Pigments are supplied with a large particle size that needs to be broken down to particle sizes less than 20 µm (Hunger and Schmidt 2019). The reduction in the particle size of the pigment contributes to the overall appearance of the coating by improving the gloss, opacity and the performance of the coating.

The methods of pigment dispersion use either high speed dispersers, ceramics or glass beads. Improper pigment stabilization can lead to issues such as “pigment shock,” where particles re-agglomerate, as illustrated in **Figure 2.9** (Hunger and Schmidt 2019).

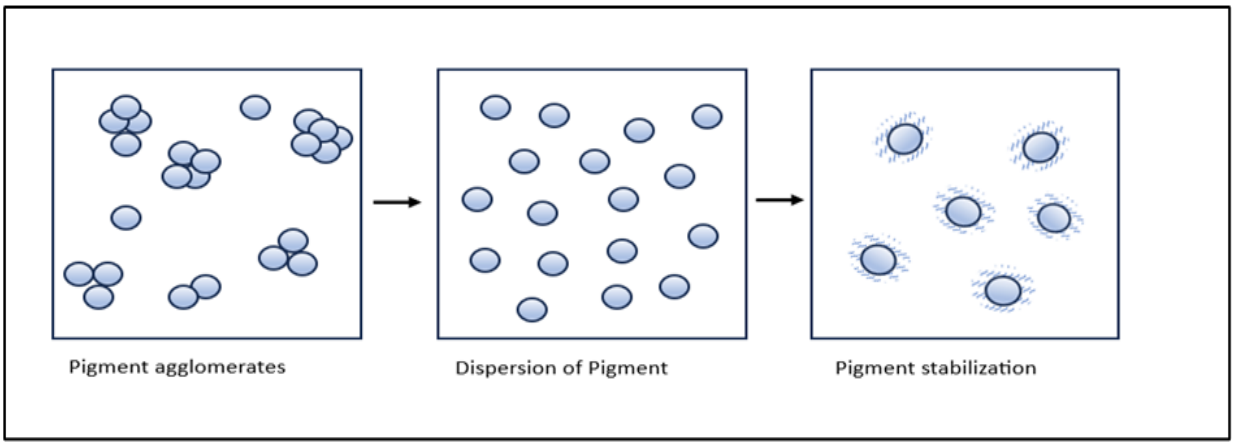

Figure 2:9. Dispersion of pigments.

2.1.11) Film formation

Coatings dry either through solvent evaporation, a process known as oxidation, or through chemical reactions in which the base and hardener crosslink to form a strong, durable protective film. (**Figure 2.10)** (Lyon, Bingham and Mills 2017).

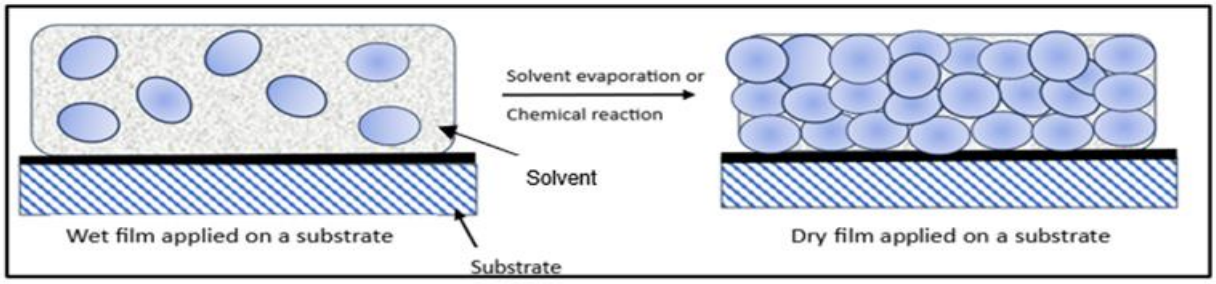

Figure 2:10. Formation of a coating film.

2.1.12) Manufacturing process for anti-corrosive coatings

The manufacturing process of an anti-corrosive coating (**Figure 2.11**) involves a series of steps to produce high-quality, stable coating tailored to specific applications. This begins with the selection of raw materials, including pigments for colour and opacity, binders for film formation and adhesion, solvents to adjust viscosity, and

additives that enhance properties like drying time, durability, and resistance to environmental factors such as corrosion (Xia *et al.* 2023).

Production starts with weighing out the raw materials according to the manufacture's instruction followed by the premixing phase, where raw materials such as the binder, solvent and wetting and dispersing additives are blended in at low-speed agitation in large mixing tanks to create a homogeneous base, followed by the slow addition of pigments and extenders. Once all the powders are added, high-speed agitation initiates the milling and dispersion process of the pigment extenders. (Maile, Pfaff and Reynders 2005).

The mill base would be checked for dispersion of pigment-particle sizes, leading to the subsequent let-down stage, by the incorporation of additional binders, solvents, and additives to achieve the desired viscosity and other performance characteristics.

Key properties, such as colour accuracy, adhesion, gloss, and drying time are tested by the quality control team ensuring that the product meets industry standards (Lyon, Bingham and Mills 2017). Once approved, the paint is filtered to remove impurities, then filled and packaged in various container sizes. The finished products are stored under specific conditions to ensure stability and optimal shelf life before distribution (Low *et al.* 2023).

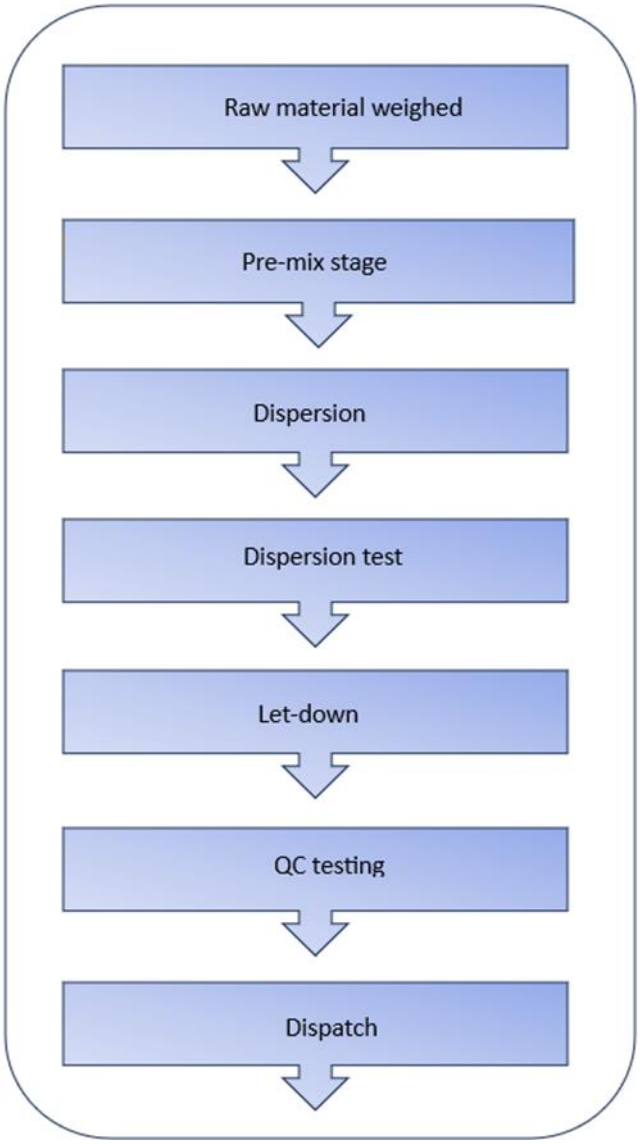

Figure 2:11. Paint manufacture processes.

2.2) Nanomaterials as anti-corrosive additives

Corrosion inhibitors as nanomaterials are advanced substances engineered at the nanoscale to prevent metal corrosion. Nanomaterials are defined as materials with at least one dimension between 0.1 - 100 nm in three-dimensional space (Mekuye and Abera 2023). These inhibitors often enhance protection by forming protective layers or interacting with metal surfaces more effectively due to their high surface area and reactivity. Examples of nanoparticles are zinc phosphate, graphene oxide, and polyvinylpyrrolidone which are integrated into coating formulation for improved corrosion resistance (Biswal *et al.* 2021; Zhang and Zhu 2021; An *et al.* 2023).

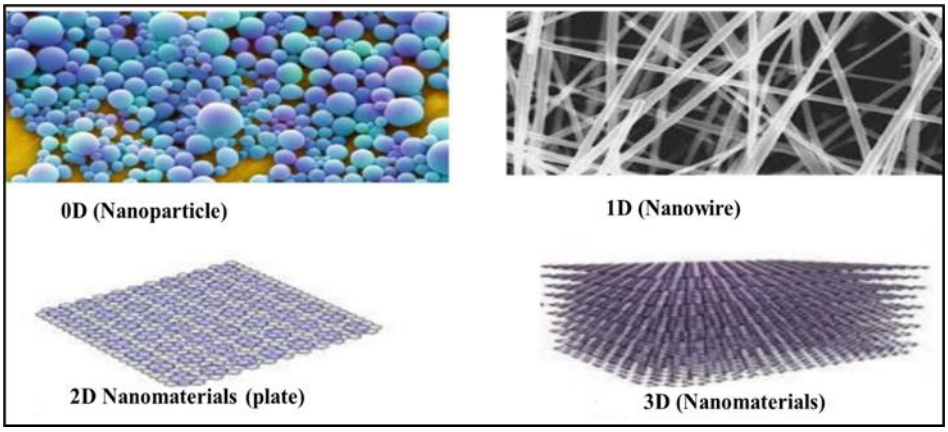

Figure 2:12. Classification of nanomaterials (Ali Salman 2020).

Nanomaterials are categorized on the basis of their dimensional attributes, leading to classifications such as zero-dimensional (0D), one-dimensional (1D), two-dimensional (2D), and three-dimensional (3D) classifications **(Figure 2.12)**. Zero-dimensional nanomaterials, have all dimensions within the nanoscale. They are often used to enhance the properties of coatings by filling pores and creating dense crosslinked networks that improve mechanical stability and corrosion resistance (Yao *et al.* 2022).

Zero-dimensional nanomaterials have all three dimensions (length, width, and height) confined to the nanoscale (typically less than 100 nm). Examples include nanoparticles and quantum dots (Wang *et al.* 2022).

One-dimensional nanomaterials, such as nanowires, possess nanoscale dimensions along two axes and can form dense layers when integrated into coatings, preventing the infiltration of corrosive substances. These nanomaterials often exhibit superior electrical and mechanical properties, making them useful in applications where enhanced durability and electrical conductivity are required (Indu *et al.* 2020).

Two-dimensional nanomaterials, including graphene and other nanosheets, are characterized by their layered structures, where atoms are bonded within layers with van der Waals forces between them. These materials are particularly effective at improving the barrier properties of coatings, as their structures can impede the penetration of corrosive elements. However, their dispersion within polymers can be

challenging, necessitating modifications to improve compatibility (Necolau and Pandele 2020; Liu *et al.* 2022; Chen *et al.* 2023).

Three-dimensional nanomaterials are less confined by nanoscale dimensions and include structures such as bulk powders and multi-layered nanocomposites. These materials can combine the properties of various nanomaterials, leading to synergistic enhancements in their performance.

2.3) Zinc phosphate

Zinc phosphate ($Zn_3(PO_4)_2$) is widely recognized as a non-toxic, anti-corrosive nanomaterial that offers an eco-friendly alternative to strontium chromates. While strontium chromates have traditionally been used in solvent-borne coatings for their excellent anti-corrosive properties, they pose significant environmental hazards. In contrast, zinc phosphate's low toxicity and biodegradability make it a safer option for applications such as corrosion control and water treatment. However, despite its relatively benign profile, zinc phosphate is still subject to environmental and safety regulations because of its long-term impacts on aquatic ecosystems. It is classified under the EU's Global Harmonized System (GHS) as risk category 1/H410, indicating high toxicity to aquatic life. As environmental concerns continue to grow, further developments are needed to improve its performance while reducing ecological risks (Gimeno L 2014; Information 2024).

$Zn_3(PO_4)_2$, (**Figure 2.13**), supplied as a white-beige inorganic powder, crystallizes in a rhombic conformation. Its low solubility in water and alcohol makes it a suitable candidate for anti-corrosive coatings. $Zn_3(PO_4)_2$ is very stable and versatile and can be used in a variety of anti-corrosive coating formulations, including Water-borne and solvent-based binders, epoxies, and alkyds; however, the particle size should not exceed 4–5µm to maintain optimal performance (Knudsen and Forsgren 2017).

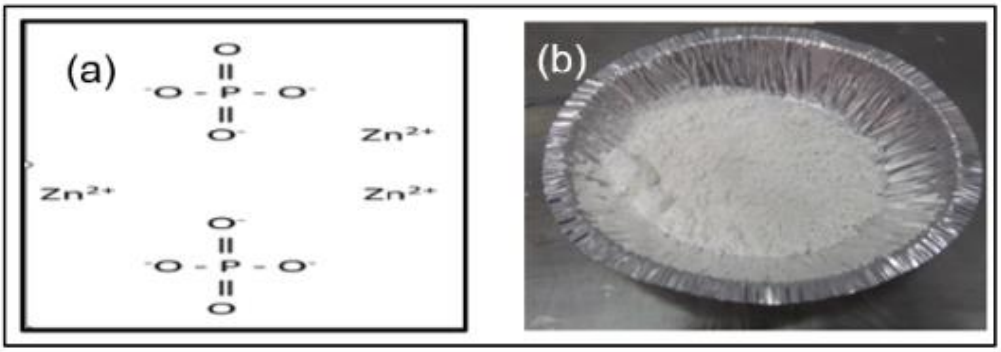

Figure 2:13. Illustration of **(a)** chemical formula of zinc phosphate; **(b)** industrial grade of zinc phosphate as supplied

2.3.1) Mechanism of corrosion inhibition by zinc phosphate

The protective action of $Zn_3(PO_4)_2$, is attributed mainly to the formation of a passive layer on the metal surface. In a humid atmosphere, phosphate ions are released, leading to the formation of zinc-iron phosphate hydrate ($Zn_2Fe(PO_4)_2 \cdot xH_2O$) on ferrous substrates. This layer significantly hinders the corrosion process by forming a protective barrier that limits further diffusion of aggressive species (Knudsen and Forsgren 2017). Gimeno *et al.* (2016), reported that the formation of this protective layer is further enhanced by the polarization of the substrate, which plays a vital role in corrosion inhibition. Yang *et al.* (2022) reported a comparative study of three coating systems: $Zn_3(PO_4)_2$ was incorporated into polyester/TGIC (triglycidyl isocyanurate), polyester/TGIC with $BaSO_4$, and epoxy/DICY (dicyandiamide) systems. The results showed that the combination of 2% $Zn_3(PO_4)_2$ with $BaSO_4$ filler in the polyester/TGIC system provided the best performance, both in salt spray tests and electrochemical evaluations.

In addition, Yang *et al.* (2022) reported and confirmed that neutral salt spray and electrochemical tests are critical for assessing the effectiveness of $Zn_3(PO_4)_2$ containing coatings. Although salt spray tests are common in industrial applications, they do not provide detailed insights into the mechanisms of corrosion inhibition. Electrochemical techniques, such as open-circuit potential (OCP) and linear polarization resistance (LPR) measurements, offer a more detailed understanding of the coating's protective behaviour, especially during immersion tests.

The above studies (Gimeno *et al.* 2016; Yang *et al.* 2022) demonstrate the potential combination of $Zn_3(PO_4)_2$ with other additives, such as molybdenum and silica, to further enhance its anti-corrosive properties.

2.4) Graphene

Graphene is a 2D structure composed of a single layer of carbon atoms arranged in a honeycomb lattice (**Figure 2.14**). This configuration allows graphene to have a delocalized π-electron cloud, which extends across the entire structure, creating a network of aromatic C=C bonds. These bonds allow for flexibility, making the material robust due to the strong nature of its bonding structure. One of the primary motivations for studying the anti-corrosion properties of graphene is its chemical inertness, attributed to the delocalized electrons, which enable it to withstand highly corrosive environments and extreme pressures. Studies have demonstrated that monolayer graphene is impermeable, with Bunch *et al.* (2008) reporting that even standard gases, such as helium, cannot penetrate a single graphene layer.

However, graphene oxide (GO) is an oxidized derivative of graphene. GO is characterized by various physicochemical properties, including its nanoscale size, high surface area, and electrical charge. Unlike graphene, GO is less conductive than graphene, has better insulating properties and acts as an insulator. Its mechanical properties also differ significantly from graphene, making GO a structurally weaker material.

GO is typically produced using the modified Hummers' method, where the addition of functional groups makes it strongly hydrophilic, allowing for good dispersibility in water and other solvents. Additionally, these oxygen-containing functional groups give GO the potential for covalent functionalization, particularly with amine-containing materials, which can enhance the properties of GO composites and coatings.

Wang *et al.* (2022) investigated the anti-corrosive properties of a novel water-borne epoxy coating reinforced with graphene for steel protection in a NaCl environment. By leveraging the permeability of graphene to atoms and molecules, researchers have incorporated it into coatings to significantly enhance corrosion resistance (Necolau and Pandele 2020). To improve the dispersibility of graphene and prevent

the formation of a conductive network, chemical modifications and precise graphene orientation were implemented. The resulting doped carbon quantum dots with modified graphene in a water-borne epoxy (NCQDs@Gr/WEP) composite coating were characterized using FTIR, X-ray diffraction (XRD), and SEM. After 10 days of immersion in a saline solution, the NCQDs@Gr/WEP composite coating maintained an impedance value of 10^{10} Ω·cm², approximately three orders of magnitude greater than that of the unmodified epoxy coating. The enhanced protection was attributed to improved interfacial interactions and the formation of a stable protective layer on the steel surface (Yao *et al.* 2022).

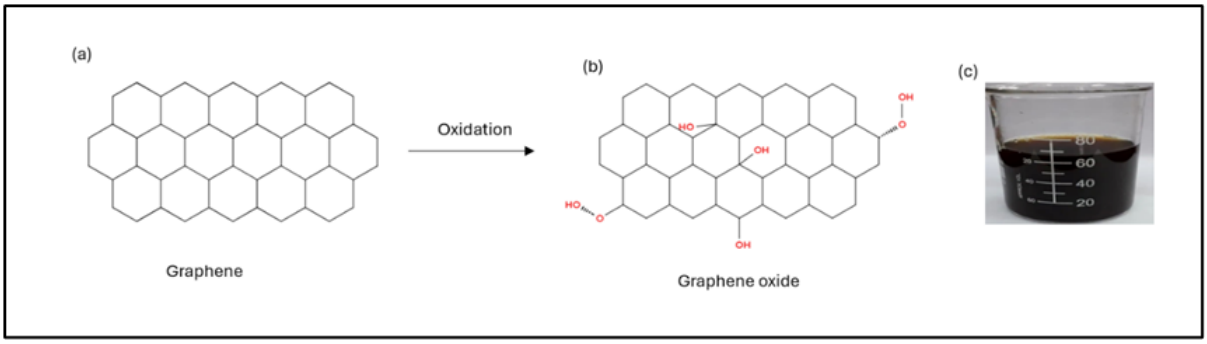

Figure 2:14. Structures of **(a)** graphene, **(b)** graphene oxide and **(c)** graphene oxide suspension.

2.4.1) Mechanism and modification enhancements of GO for improved anti-corrosive coatings

Research on GO has shown promising results in enhancing the corrosion protection performance of coatings. Parhizkar, Ramezanzadeh and Shahrabi (2018) studied the effect of incorporating GO into silane coatings and compared functionalized and non-functionalized GO. They discovered that functionalized GO, with groups like amines, improved coating adhesion and reduced corrosion by forming covalent bonds with silane, effectively blocking pores and preventing water and ion penetration. In contrast, non-functionalized GO has little effect on the effectiveness of the coating.

Similarly, Taheri, Ramezanzadeh and Mahdavian (2019) reported that the functionalization of GO with amines significantly improved the performance of epoxy coatings. Functionalized GO, was successfully intercalated within the epoxy matrix, enhancing ionic resistance and reducing chloride ion uptake. Pourhashem *et al.*

(2020) highlighted the importance of achieving homogeneous dispersion of GO within coatings. They reported that excessive GO concentration led to agglomeration, diminishing the barrier properties of the epoxy resin.

2.5) Polyvinylpyrrolidone

Polyvinylpyrrolidone (PVP), also known as polyvidone or povidone, is a versatile, water-soluble synthetic polymer, produced via free-radical polymerization of the monomer N-vinylpyrrolidone (Abdulhadi *et al.* 2023). In its dry form, PVP appears as an off-white, hygroscopic powder capable of absorbing up to 40% of its weight in water, making it highly effective in moisture-sensitive applications. PVP is a linear chain polymer, that has a one-dimensional structure but can promote two-dimensional (2D) crystal growth in zinc oxide (ZnO) (**Figure 2.15**) (Abdulhadi *et al.* 2023).

PVP has a range of applications across various industries. In biomedical research, it serves as a stabilizing agent for proteins, enzymes, and other biological substances. Its role as a stabilizer ensures the functionality and longevity of biomolecules in research and therapeutic applications. PVP is also utilized in wastewater treatment to remove heavy metal cations, highlighting its environmental significance (John, Kuruvilla and Joseph 2013).

In materials science, PVP is recognized for its excellent wetting properties and ability to form thin, uniform films, making it an ideal additive in coatings (John, Kuruvilla and Joseph 2013; Abdulhadi *et al.* 2023).

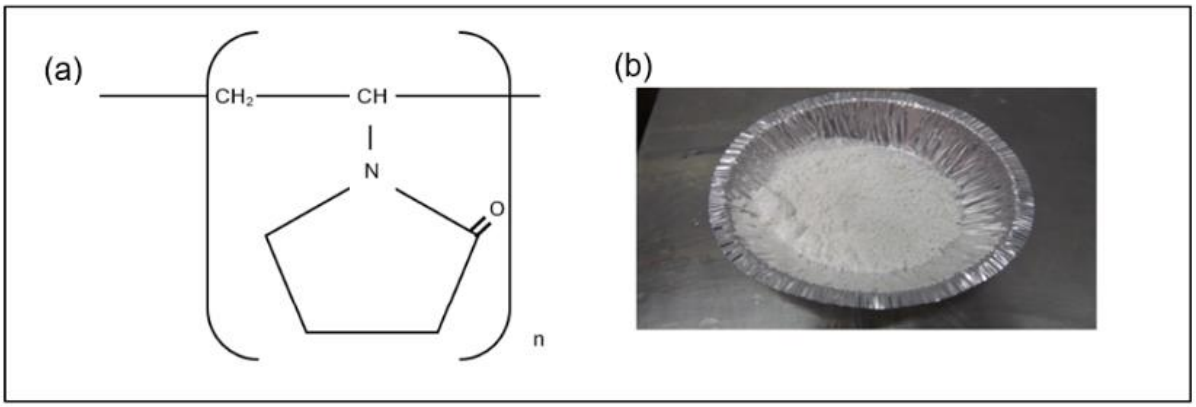

Figure 2:15. Structures of **(a)** polyvinylpyrrolidone and **(b)** polyvinylpyrrolidone as a dry powder.

2.5.1) Mechanism and modification of PVP for improved anti-corrosive coatings

Polyvinylpyrrolidone (PVP) has proven to be an effective corrosion inhibitor, particularly for mild steel in acidic environments. Studies have examined its inhibitory properties, establishing that PVP acts as a mixed-type inhibitor, impacting both anodic and cathodic reactions. In acidic media such as H_2SO_4 and HCl solutions, PVP enhances corrosion resistance by forming a protective layer on the metal surface. This layer serves as a barrier that obstructs both mass and charge transfer, which are the primary processes, driving corrosion (Abdulhadi *et al.* 2023). The inhibition efficiency of PVP is attributed to its ability to adsorb onto the metal surface, forming a protective film that reduces both the double-layer capacitance and the charge-transfer resistance. Electrochemical studies, including potentiodynamic polarization and electrochemical impedance spectroscopy (EIS), confirm this behaviour (John, Kuruvilla and Joseph 2013). PVP adsorption is consistent with the Langmuir adsorption isotherm, suggesting that PVP molecules uniformly cover the metal surface, preventing aggressive ions from interacting with the steel (Al Juhaiman, Mustafa and Mekhamer 2012; Abdulhadi *et al.* 2023). The structure of the polymer, specifically its carbonyl and methylene group, contains oxygen atoms with lone electron pairs. These atoms facilitate the adsorption process by creating strong interactions between PVP and the metal surface (Teodorescu and Bercea 2015). This chelation strengthens the protective properties of PVP, making it effective in both aqueous and polar organic media. The water-solubility of PVP and its ability to form stable films in acidic environments further contribute to its corrosion inhibition potential (John, Kuruvilla and Joseph 2013; Abdulhadi *et al.* 2023).

PVP is concentration-dependent, as the concentration of PVP increases, so does its inhibition efficiency, until it reaches an optimal concentration, where the metal surface is saturated with PVP molecules. At this stage, increasing the concentration of PVP, provides only minimal additional protection. (John, Kuruvilla and Joseph 2013). However, at higher temperatures, the efficiency of PVP decreases due to the

weakening of adsorption bonds between PVP and the metal, resulting in desorption and diminished corrosion protection (Al Juhaiman, Mustafa and Mekhamer 2012).

Comparisons between PVP and other polymeric inhibitors, such as polyethylene glycol (PEG), have shown that while both exhibit strong inhibition properties, PVP performs better in terms of adsorption and film formation, especially in neutral and acidic media (John, Kuruvilla and Joseph 2013). Its hygroscopic nature allows PVP to absorb up to 40% of its weight in water, which is advantageous in wet environments (Al Juhaiman, Mustafa and Mekhamer 2012). The ability of PVP to chelate with metal ions further enhances its inhibition efficiency (Teodorescu and Bercea 2015).

EIS studies consistently show that PVP adsorption leads to the formation of a thicker electronic double layer at the steel/solution interface, increasing the stability of the protective barrier and improving corrosion resistance (John, Kuruvilla and Joseph 2013). PVP's mixed-type inhibition mechanism reduces the dissolution of iron and slows the cathodic hydrogen evolution reaction, making it highly effective in a variety of corrosive environments (Al Juhaiman, Mustafa and Mekhamer 2012).

PVP has emerged as a promising corrosion inhibitor, particularly in acidic media. Its adsorption ability, concentration-dependent efficiency, and ability to form protective films significantly enhance its charge-transfer resistance and reduce its double-layer capacitance. However, its efficiency diminishes at higher temperatures. Owing to the low toxicity of PVP, it is a viable alternative to traditional, more hazardous inorganic inhibitors. This environmentally friendly profile positions PVP as an attractive green inhibitor for industries seeking to adopt sustainable corrosion protection methods (Al Juhaiman, Mustafa and Mekhamer 2012; Abdulhadi *et al.* 2023).

CHAPTER 3 - THEORETICAL PRINCIPLES

This chapter focuses on the theoretical principles involving the analytical characterization techniques used in this research, followed by the electrochemical theoretical principles of EIS and PDP and a brief overview of theoretical principles associated with stimulated, industrial accelerated corrosion.

3.1) Fourier transform infrared (FTIR) spectroscopy

Fourier-transform infrared (FTIR) spectroscopy is a fast and highly versatile technique used to analyze organic and inorganic compounds. It helps assess the degradation of organic coatings by measuring light absorption at specific wavelengths, which correspond to the atom-atom vibrational energy of a molecular bond. The fingerprint region forms when infrared radiation passes through a sample, causing the absorption of specific wavelengths. (Berthomieu and Hienerwadel 2009). A typical schematic diagram of a modern FTIR spectrometer is represented in **Figure 3:1**.

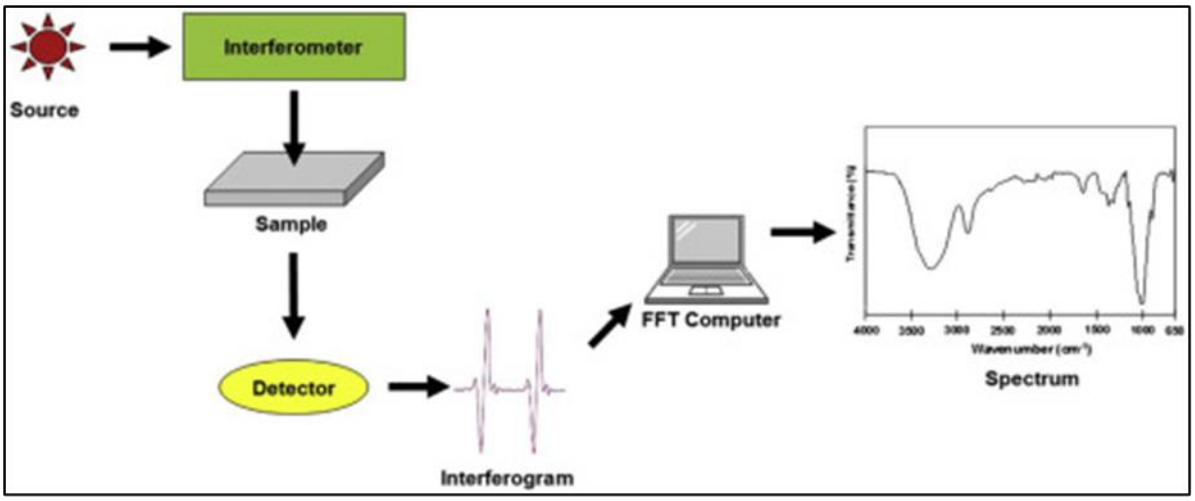

Figure 3:1. Schematic illustration of FTIR principle (Undavalli, Ling and Khandelwal 2021).

3.2) X-ray diffraction (XRD)

X-ray diffraction (XRD) is a rapid, non-destructive analytical technique widely used to determine the crystallographic structure of materials. It provides valuable information about unit cell dimensions, and can be used to study the physical and chemical properties of various crystalline materials, such as powders, thin films and bulk solids (Epp 2016).

3.3) Field emission scanning electron microscopy (FESEM)

Field Emission Scanning Electron Microscopy (FESEM) is a high-resolution technique for analyzing surface morphologies. It is ideal for examining the topography of materials and coatings. A focused electron beam interacts with the sample's surface, producing secondary and backscattered electrons, that reveal surface features, irregularities, protrusions and coating adherence.

FESEM detects nanoscale features essential for assessing anti-corrosive coatings. Rough or flake-like structures seen in images can suggest interactions within the coating, that improve corrosion resistance. FESEM can detect microstructural changes resulting from coatings and surface treatments. (Lewczuk and Szyryńska 2021).

3.4) Energy dispersive X-Ray spectroscopy (EDX)

Energy dispersive X-ray spectroscopy (EDX), often used alongside FESEM, identifies the elemental composition of materials. EDX detects X-rays emitted from a sample when struck by an electron beam, confirming the presence or absence of corrosion-related elements like iron oxides. It also verifies the successful deposition of coating materials such as zinc phosphate, graphene oxide, or polymer films. These technique provides a qualitative and semi-quantitative data, to assess the uniformity of coatings (Allen *et al.* 2012).

3.5) Optical Profilometry

Optical profilometry is a non-contact technique that measures the surface roughness and topography by analysing light reflections from the material's surface. This method generates 2D and 3D surface maps to show the roughness variations. Optical profilometry measures surface changes, by calculating root mean square (RMS) roughness. These measurements dictate how much the surface height varies on average, indicating how smooth or rough the surface is. These variations indicate how well coatings, act as barriers against corrosion. It also assesses the coating thickness and coating uniformity affecting corrosion resistance. With high precision and the ability to analyse large areas, it is a key tool for materials characterization. (Dallaire, Dufour and Gauthier 1993).

3.6) Electrochemical impedance spectroscopy (EIS)

Electrochemical Impedance Spectroscopy (EIS) **(figure 3.2)** is a versatile, non-destructive method that measures a system's resistance to electrical flow over a range of frequenciese. EIS uses a three-electrode setup: the working electrode, the counter electrode, and the reference electrode. This technique helps researchers study electrode behavior, material conductivity, and surface properties, especially in nanomaterials. Because of this, EIS is widely used in corrosion analysis, battery research, and sensor technologies (Rouya *et al.* 2012; Magar, Hassan and Mulchandani 2021).

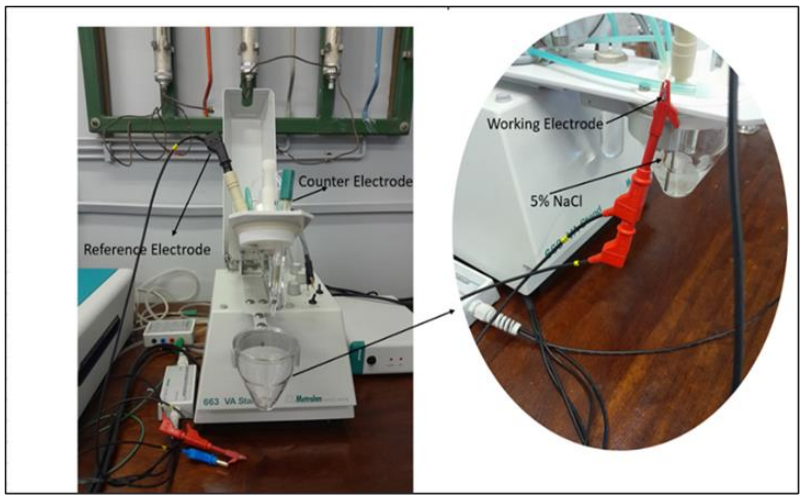

Figure 3:2. The electrochemical three-electrode system.

3.7) Potentiodynamic polarization (PDP)

Potentiodynamic Polarization (PDP) is a fast electrochemical method, that measures the current response of a material to a small, applied potential, enabling rapid determination of corrosion rates. This method, provides data for adjusting processes, testing inhibitors, and assessing pitting susceptibility. In addition to giving the corrosion rate, PDP helps identify key parameters like corrosion potential and Tafel slopes, which offer insights into passivation behavior and localized corrosion risks. By analyzing both anodic and cathodic behaviors of the coating, PDP yields key parameters such as corrosion potential (E_{corr}) and corrosion current density (I_{corr}), which offer insights into passivation and localized corrosion. EIS and PDP when combined, offers an invaluable data for optimizing protective coatings and improving material performance in various environments.

EIS and PDP, when combined, provides a comprehensive understanding of corrosion processes. These techniques complement each and offers essential data for optimizing protective coatings and improving material performances across various environments. These techniques work in tandem to assess the effectiveness of coatings and inhibitors.

3.8) Salt spray

The salt spray test chamber is specifically designed to simulate outdoor environmental conditions for testing the anti-corrosion properties of materials with surface coatings such as paint, electroplating, and other protective films. These chambers adhere to international testing standards, such as ASTM B117, ensuring reliable performance and reproducibility in corrosion resistance assessments **(Figure 3:3).**

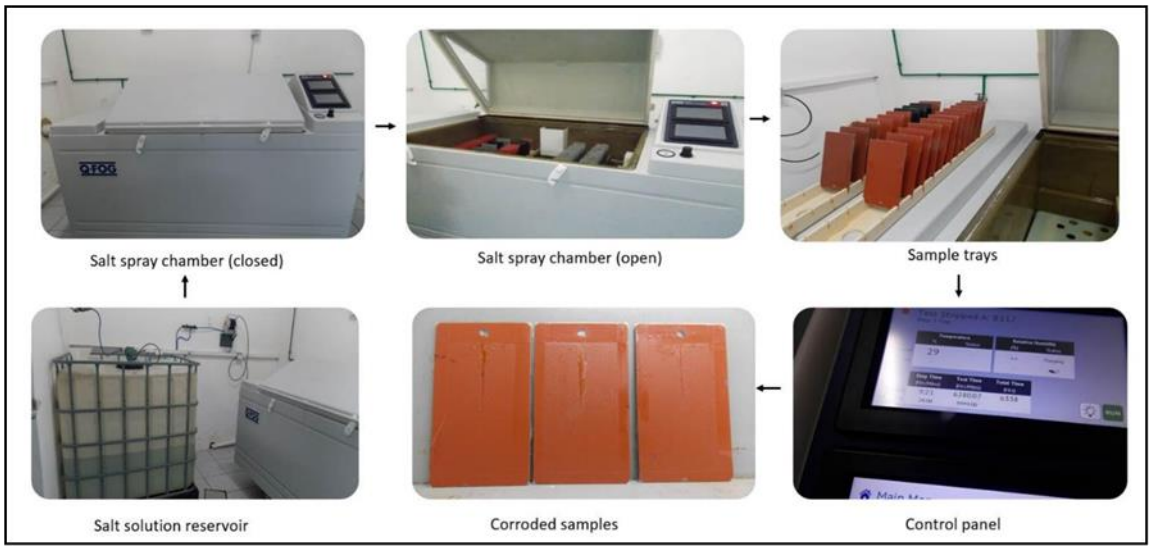

Figure 3:3. Illustration of a salt spray chamber adhering to test method ASTM B117.

Salt spray testing remains one of the most standardized and widely used methods for assessing corrosion resistance. Salt spray tests, such as the Q-FOG SSP corrosion tester, can perform continuous accelerated corrosion tests. These tests expose materials to a corrosive environment in a controlled manner (Ramoškienė, Gladkovas and Šalkauskas 2003). This method allows for the exposure of samples to alternating wet and dry conditions, which more accurately mimics real-world environments. This process replicates the effects of rain, humidity, and dry conditions, thereby providing a more accurate assessment of long-term corrosion behaviour. Cyclic corrosion testing has been shown to yield results comparable to those observed in outdoor exposures, providing insights into the structure, morphology, and corrosion rates of tested materials (Hare 1995).

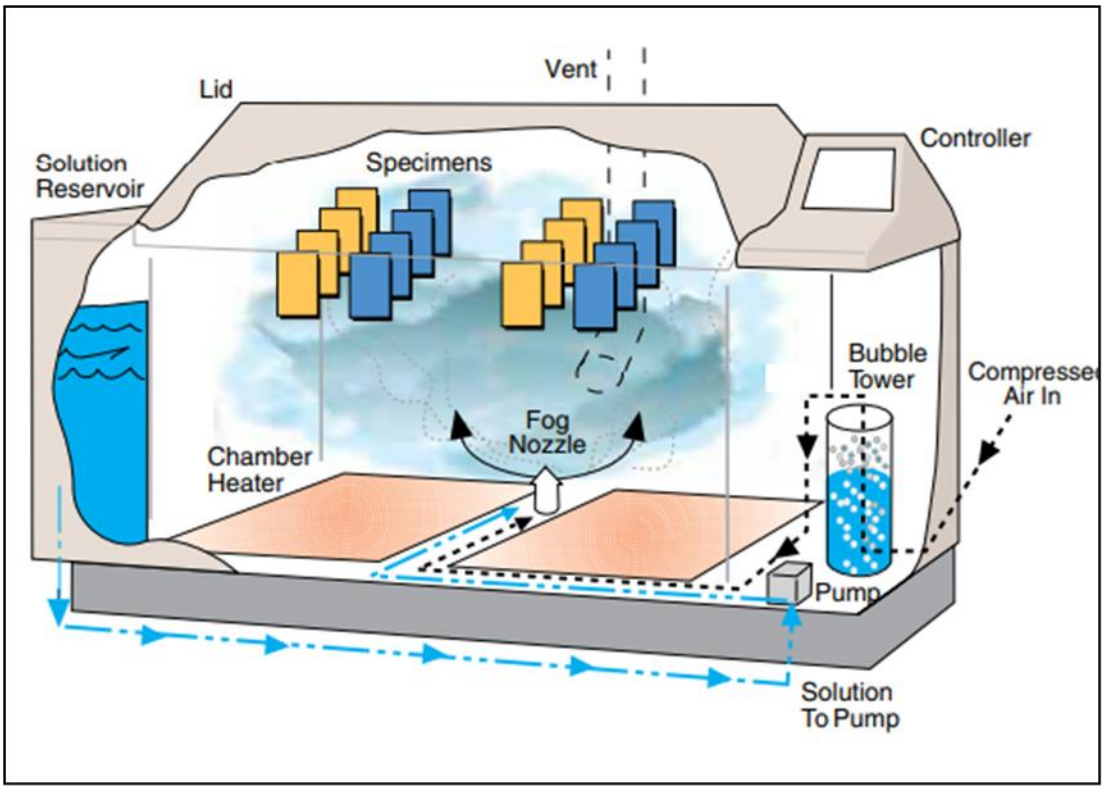

Figure 3:4. Schematic illustration detailing the operation mechanism of a salt spray chamber(Q-lab 2024).

The mechanism of the salt spray chamber is illustrated in **Figure 3:4**. During the fog function of the salt spray tester, the internal reservoir pumps a corrosive electrolyte solution to the nozzle, which atomizes the solution into a fine mist. This mist fills the chamber, enveloping the test samples. To ensure uniform testing conditions, compressed air is passed through a humidifying bubble tower, while the chamber heaters maintain a constant temperature, following the programmed parameters for the test (Ijsseling 1989).

The accelerated ss exposes materials to corrosive conditions, leading to the formation of corrosive products such as oxides over time. The duration of the test, is adjusted based on the sample's corrosion resistance, making it a flexible method for comparing different materials. As a result, industries like automotive, aerospace, and manufacturing rely on this approach to evaluate the effectiveness of surface and coatings treatments. (Singleton 2010).

3.9) Accelerated artificial weathering testing

The QUV accelerated weathering tester is designed to replicate the environmental conditions that reproduces the damage that materials experience outdoors caused by sunlight, rain and dew (**Figure 3.5**). Accelerated weather testers can simulate years of material degradation caused by outdoor exposure within weeks or months. These devices support compliance with international standards such as ISO 4892 and ASTM G154, which outline procedures for artificial weathering using fluorescent UV lamps. Industries including construction, automotive, and coatings rely on these tests to predict material lifespan, ensure product reliability, and optimize formulations to meet performance standards (Q-lab 2024).

The QUV accelerated weathering tester simulates environmental factors like sunlight, moisture, and temperature variations to expedite material aging, enabling researchers to evaluate durability in a shorter timeframe compared to natural outdoor exposure (Q-lab 2024).

UV Light Simulation:

The tester employs UVA-340 and UVB-313 fluorescent lamps to replicate the sun's ultraviolet spectrum. UVA-340 lamps accurately mimic the short-wavelength UV portion (295–365 nm) of sunlight, which is particularly harmful to durable materials like plastics and coatings. UVB-313 lamps emit even shorter wavelengths, accelerating the photodegradation process for materials highly resistant to UV radiation (Q-lab 2024).

Moisture Simulation:

To replicate dew and rain, the QUV tester uses condensation and water spray mechanisms, exposing materials to cycles of wetness and dryness that contribute to degradation.

Temperature Control:

A black panel thermometer within the chamber regulates temperature, ensuring consistent conditions that closely mimic real-world scenarios.

The solar eye Irradiance Control system maintains consistent UV light intensity by monitoring and adjusting lamp power, compensating for lamp aging and ensuring reproducible test conditions.

By integrating these components, the QUV tester provides a controlled environment to assess material performance under simulated environmental stresses, aiding in predicting product lifespan and ensuring reliability across various industries (Rabek 2012).

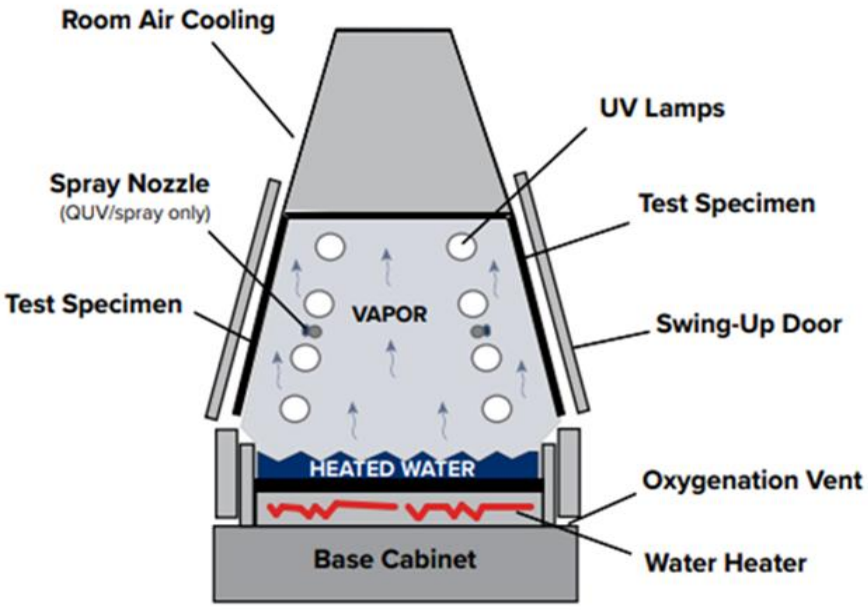

Figure 3:5. Principle of QUV accelerated weathering tester during the condensation cycle (Q-lab 2024).

CHAPTER 4 - MATERIALS AND METHODS

This chapter describes the materials and methods used for the experiments implemented in this study.

4.1) Materials and methods

4.1.1) Materials

Graphene oxide (4 mg/ml) was dispersed in H_2O, and polyvinylpyrrolidone (PVP), with an average mol wt.=40.000, were purchased from Sigma-Aldrich. Zinc phosphate was purchased commercially from an industrial raw material supplier. Zinc phosphate. In addition to the additives, pigments, resins, and solvents required to make up the WBA composite were purchased from different raw industrial material suppliers.

Salt spray corrosion experiments were performed using mild steel (MS) as a substrate purchased from Q-Lab. The type r-36 matt was finished from cold-rolled MS and had dimensions of 75 x 0.81 x 152 mm.

4.1.2) Fabrication of water-borne acrylic nanomaterial composites

Several different formulations containing water-borne acrylic (WBA) composites were prepared for comparative analysis. The specific quantities of raw materials used in the formulation are not disclosed owing to proprietary rights:

- WBA - $Zn_3(PO_4)_2$: Containing 5% $Zn_3(PO_4)_2$
- WBA - GO: Containing 5% GO
- WBA – PVP: Containing 5% PVP
- WBA - GO/PVP: Containing 2.5% GO and 2.5% PVP
- WBA - $Zn_3(PO_4)_2$/ PVP: Containing 2.5% $Zn_3(PO_4)_2$ and 2.5% PVP

4.1.3) Fabrication of WBA containing - $Zn_3(PO_4)_2$

A known quantity of the wetting and dispersing additives was weighed on an analytical scale and transferred to a container filled with a known amount of water. This mixture was stirred using a Cowles high speed mixer at 1000 rpm for 5 minutes. A known amount of weighed pigments (red oxide, calcium carbonate, and talc) was slowly introduced into the solution forming a mill base. The pigments were weighed using an analytical balance. Five percent anti-corrosive material, $Zn_3(PO_4)_2$, was then added. The mixture was homogenized using the Cowles mixer at 2000 rpm until the particle size of the mill-base was reduced to less than 30 µm, as confirmed by a Hegman gauge as illustrated in **Figure 4:1(d)** (Mariz *et al.* 2010). **Figure 4:1** demonstrates the method for making a water-borne acrylic anti-corrosive composite.

Once the particle size of the mill-base was reduced to less than 30 µm, a measured amount of acrylic Water-borne resin, coalescing solvents, and water was gradually incorporated into the mill-base mixture. Coating quality was measured on each coating characteristics and its performance. The key characteristics for determining the coating quality was fineness of grind, colour, opacity, durability and drying time.

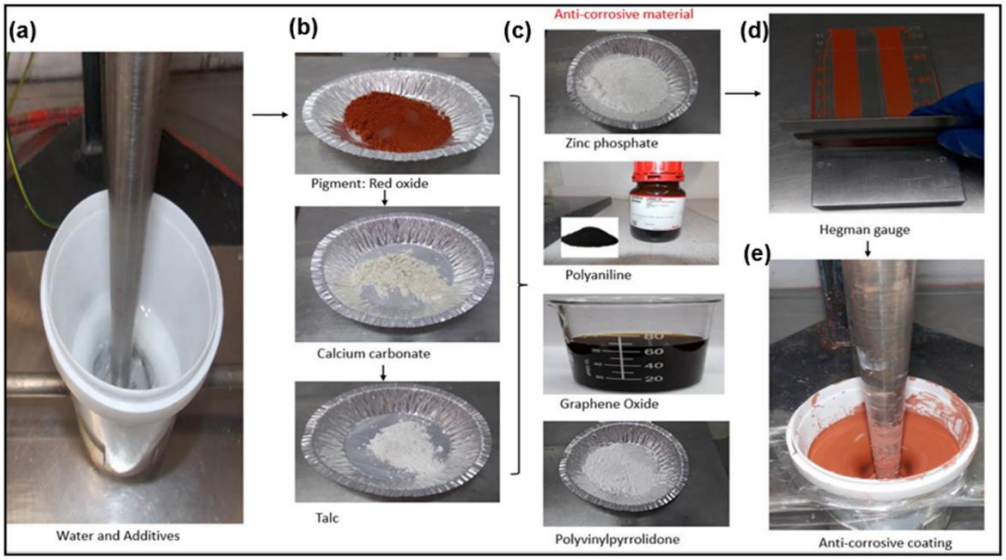

Figure 4:1. Fabrication of WBA anti-corrosive composites **(a)** water and additive; **(b)** pigments; **(c)** anti-corrosive nanomaterial; **(d)** Hegman Gauge; **(e)** WBA- composite.

4.1.4) Mild steel pretreatment and fabrication of the working electrodes

Mild steel (MS) panels were prepared for characterization analysis of anti-corrosive materials. Mild steel panels were then cut to a size of 10 × 0.80 × 2 mm^2. An aluminum conducting tape was affixed to the ends of the red copper fibers because of its excellent electrical conductivity. A drop of catalyzed epoxy resin was used to bond the tape to the MS. The “sandwich" tape-metal was placed in a rubber mold and the catalyzed epoxy resin was poured into the mold and left overnight at room temperature to cure, forming an electrode (**Figure 4:2).**

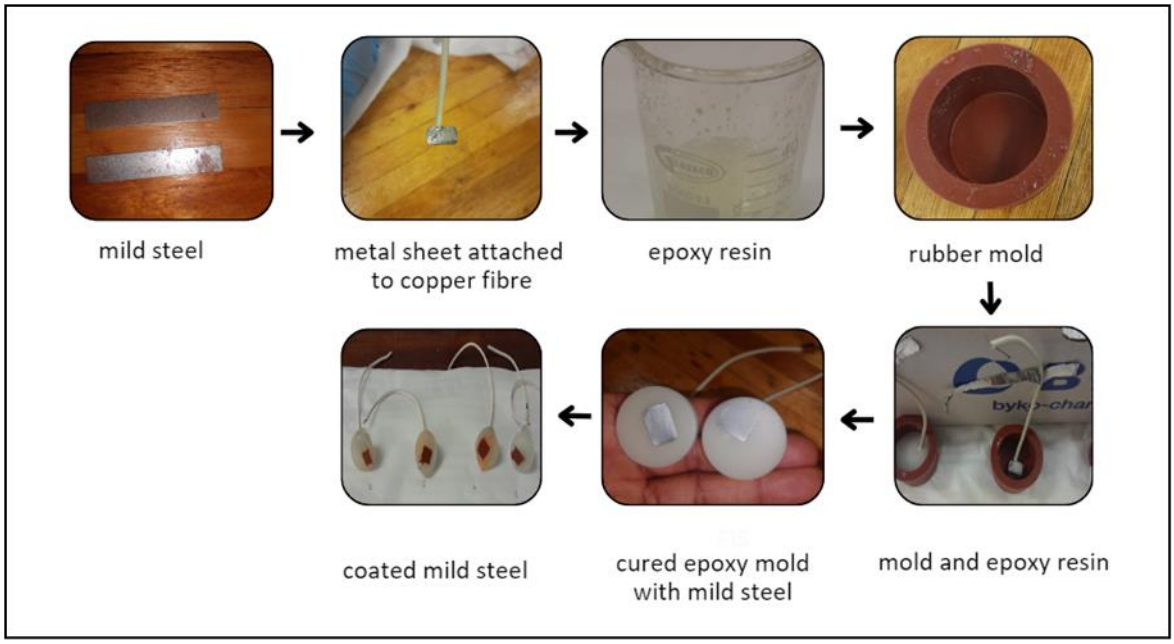

Figure 4:2. Illustration of the fabrication of working electrodes.

4.2) Characterization of anti-corrosive materials

4.2.1) Fourier-transform infrared spectroscopy (FTIR)

The structural and functional groups present in PVP, GO, $Zn_3(PO_4)_2$ and their respective water-borne acrylic-composites will be investigated using Fourier transform infrared (FTIR) spectroscopy (Perkin Elmer) over a wavelength range of 4000 to 500 cm^{-1}.

4.2.2) X-ray diffraction (XRD)

XRD was used to examine the crystal structure of the anti-corrosive nanomaterial, and their water-borne acrylic-composites. This investigation was conducted utilizing the D8 Advance diffractometer, with Cu-Kα radiation (λ = 1.5406 Å), covering an angle between 10 to 90° at 2Θ.

4.2.3) FE SEM

Scanning electron microscopy coupled with EDX spectrum and elemental mapping was preformed using SEM: APREO 2. This method was used to examine the surface morphology of the metal surface and the metal surface coated with WBA anti-corrosives coatings.

4.2.4) Optical profilometer

The optical profilometer (MicroXAM-800) and atomic force microscopy (MFP3D) was used to determine the topography of the metal surface and the metal surface coated with WBA anti-corrosives coatings.

4.3) Electrochemical corrosion assessments

Electrochemical characterization was conducted using EIS and linear polarization PDP to study the inhibitory behavior of the anticorrosive materials prepared (B. del Amo *et al.* 2002) . This application provides information on corrosion analysis such as charge transfer resistance, double-layer capacitance, and diffusion-controlled processes. EIS data are typically represented using Nyquist or Bode plots, allowing for the modelling of corrosion mechanisms through equivalent electrical circuits (Randviir and Banks 2013).

4.3.1) Electrochemical impedance spectroscopy (EIS)

Electrochemical experiments were performed using an Autolab Metrohm potentiostat PGSTAT 302 equipped with a 663A Computrace module, which was controlled via NOVA 2.1.4 software. The measurements were conducted in a three-electrode system, which consisted of a coated MS electrode as the working electrode, a silver/silver chloride (Ag/AgCl) electrode saturated with 3 M potassium chloride as the reference electrode, and a platinum electrode serving as the counter electrode. The supporting electrolyte for the system was a 5% sodium chloride solution **Figure 4:4***.*

4.3.2) EIS experiments with OCP

EIS experiments were carried out at OCPs at frequencies between 100 kHz and 0.1 Hz at an amplitude of 10 mV under steady conditions at 298 K. The system achieved a stable OCP within the first 600 s of immersion in the 5% saline solution. Therefore, a waiting period of 30 minutes before electrochemical disturbance is sufficient to ensure OCP stabilization. The EIS Nyquist spectra were fitted with an equivalent circuit model using NOVA 2.1.4 software to obtain numerical values of charge transfer (R_{ct}) and the percentage inhibition efficiency (η) of the anticorrosive materials. The semicircle diameter is correlated with the charge transfer resistance R_{ct}.

The percentage inhibition efficiency (η) of the inhibitor was calculated using **Eq. (4.1).**

$$\eta_{EIS}\,(\%) = \frac{R_{ct} - R^{o}_{ct}}{R^{o}_{ct}}\; x\; 100 \qquad (4.1)$$

where R_{ct} and R^{o}_{ct} are the charge transfer resistance with and without the inhibitors, respectively.

During an EIS experiment an alternating current (AC) signal is applied, and the system's impedance is measured. The impedance reflects the resistance of a

material to charge transfer and ion diffusion, which occurs in an electrochemical cell (Figure 3.3). When the sinusoidal AC signal is applied, the response current can be expressed with **Eq. (4.2)** and **Eq. (4.3)** (Randviir and Banks 2013):

$$Et = E_0 \sin(\omega t) \tag{4.2}$$

$$It = I_0 \sin(\omega t + \Phi) \tag{4.3}$$

where, Et is the applied potential, It is the response current, E_0 and I_0 are the initial amplitudes of potential and current, and, ω is the radial frequency (ω=2πf), Φ is the phase shift.

Nyquist plot

The EIS Nyquist spectra were fitted with an equivalent circuit model using NOVA 2.1.4 software. The frequency range in EIS experiments typically spans from 0.1 Hz to 100 kHz, generating an impedance spectrum that is often depicted in a Nyquist plot. A Nyquist plot is generated when the real part (Z) is plotted on the X-axis and the negative imaginary part (-Z) is plotted on the Y-axis is calculated **Eq. (4.4**).

The system's impedance is calculated as:

$$Z = \frac{E}{I} = Z_{0\exp(i\emptyset)=Z_0(\cos\emptyset + I\sin\emptyset)} \tag{4.4}$$

where Z, E, I, ω, and Φ are impedance, potential, current, frequency, and phase shift between E and I, respectively. The impedance is expressed in terms of a magnitude, Z_0, and a phase angle shift, Φ.

For systems with diffusion limitations, a Warburg element (W) appears as a straight line at low frequencies (Vivier and Orazem 2022). For detailed analyses, a Randle's equivalent circuit model was employed. It typically includes R_s, R_{ct}, a Warburg element (W), and a constant phase element (CPE) to account for non-ideal capacitive behaviour. Due to surface roughness and non-idealises, the CPE is often used instead of a double layer capacitor (*Cdl)*, see **Eq. (4.5))** to achieve a better electrochemical fit (Raistrick 1986; Vivier and Orazem 2022). This modelling provides

data on the system's electrochemical behaviour and allows for the interpretation of complex phenomena such as diffusion, charge transfer, and surface roughness.

$$Cdl = (Y_0 R_{CT}^{1-n})^{1/n} \quad (4.5)$$

Bode Plots

Bode plots, are an equivalent circuit models that are used electrochemical cells, and associated with the electrolyte - interface and redox reactions that are simulated as an electric circuit involving electrical components (resistors, capacitors, inductors). The impedance magnitude and phase angle often as a function of frequency as these plots are useful for analysing capacitive and resistive behaviours **Figure 4:3.**

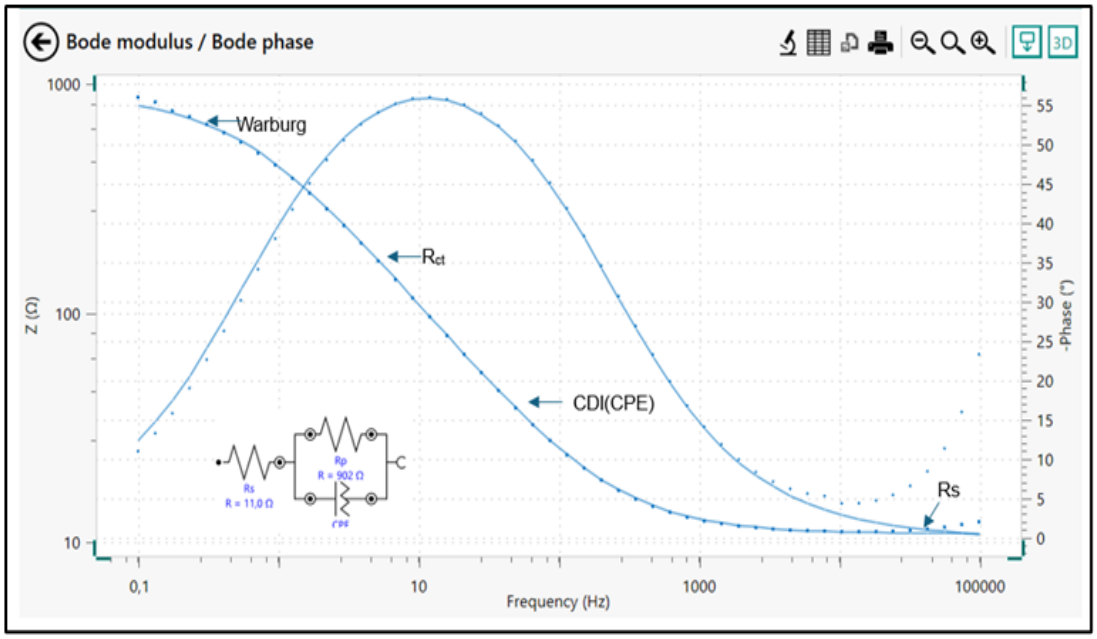

Figure 4:3. Bode plot of the impedance magnitude of the Randles equivalent model of an electrochemical interface.

4.3.3) Potentiodynamic polarization (PDP)

For polarization studies, measurements were conducted at a sweep rate of 0.166 mV/s in the potential range from –20 mV below the OCP to 20 mV above. Statistical values of the anodic and cathodic Tafel slopes ($ß_a$ and $ß_c$, respectively), corrosion potential (E_{corr}) and corrosion current (i_{corr}) were extrapolated as a straight line of the

polarization curves, whereas the percentage inhibition efficiency (η) of the nanomaterial was calculated according to **Eq. (4.6).**

$$\eta_{PDP}\ (\%) = \frac{i_{corr}^{o} - i_{corr}^{i}}{i_{corr}^{o}}\ \text{x}\ 100 \qquad (4.6)$$

where i_{corr}^{o} and i_{corr}^{i} are the corrosion current densities with and without the inhibitors, respectively.

For linear polarization resistance (LPR) measurements, experiments were conducted by applying a potential range of ±250 mV relative to the open circuit potential (OCP), with the current response recorded at a scan rate of 0.125 mV/s. The generated LPR over-potential and current values were plotted on a linear scale. The slope of these graphs was near the corrosion potential (Ecorr) that was used to determine the polarization resistance (R_p).

The inhibition efficiency (η_{LPR}) was calculated using the following equation **(Eq. (4.7)):**

$$\eta_{LPR}\ (\%) = \frac{R_P - R_P^{o}}{R_P}\ \text{x}\ 100 \qquad (4.7)$$

where: R^0p: Polarization resistance without inhibitors and Rp: Polarization resistance with inhibitors

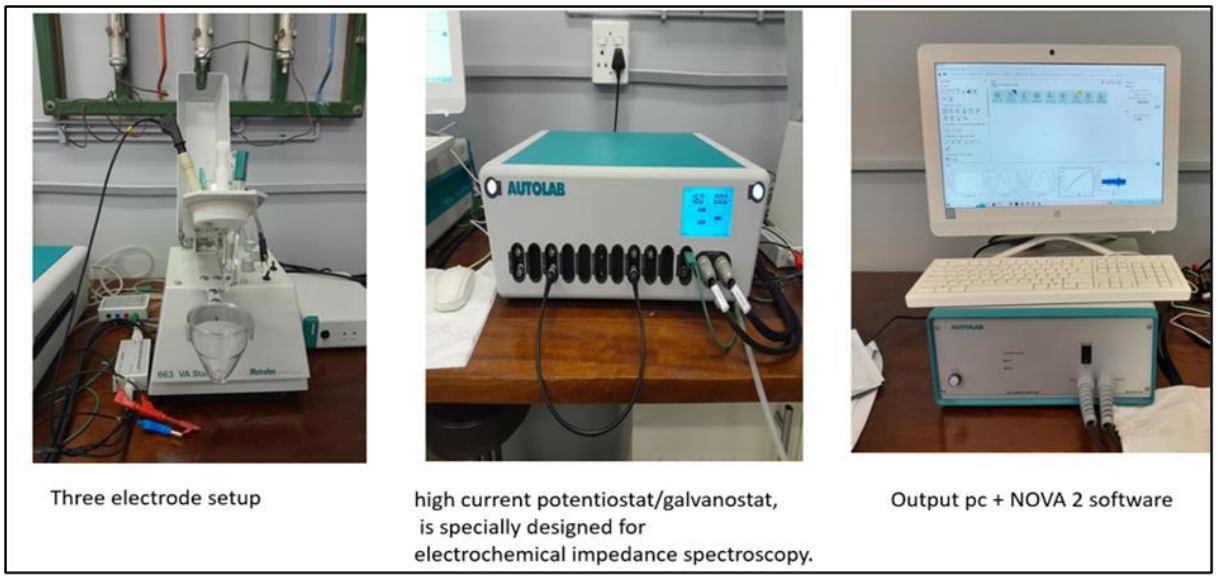

Figure 4:4. Electrochemical workstation setup for EIS and PDP experiments.

4.4) Simulated environmental testing

4.4.1) Salt spray preparation and testing

MS was purchased from Q-Lab. Type r-36 Matt finished steel panels, made from cold-rolled MS with dimensions of (75 x 0.81 x 152) mm.

The panels were degreased to remove surface contamination followed by clean water rinses. Samples of the WBA composites were adjusted to spray viscosity using water. These WBA composites were applied using a conventional air assisted spray gun (**Figure 4.5a**), with nozzle orifice: 1.5 mm and nozzle pressure: 4.0 bar.

The wet film thickness (WFT) of the coatings was 120 ±10 µm, measured with a wet film Elcometer gauge, model number 3236 (**Figure 4.5c**). The coated panels (**Figure 4.5b),** were cured for six days at ambient temperature (23°C, 50% relative humidity) and then further cured for one day in an oven at 54°C. The dry film thickness (DFT) was 15-45 µm, which was measured with a wet film Elcometer gauge, model number 456 (**Figure 4.5d**).

The panel edges were sealed with tape to prevent any exposure to air during the test. The edges of the panels were sealed with tape to prevent air exposure, as even minimal contact with air can affect the results and compromise the test accuracy.

Figure 4:5. Salt spray panel preparation, **(a)** conventional air assisted spray gun; **(b)** nano-coated material; **(c)** Dry film gauge and **(d)** WFT Guage.

Scribing of the coating

A scribe was made on the cured coating **(Figure 4:6)** to expose the underlying metal surface, leaving a bright, exposed metal line for accurate corrosion monitoring. This was done by holding the scribing tool at an angle of 90° to the surface, ensuring that only the tool's tip contacted the panel. A uniform, straight line of 5 cm in length was made, in the middle of the panel and at least 4 cm away from the panel edges. The scribing tool was inspected regularly for signs of wear, dulling, or damage, and replaced to ensure a precise scribe.

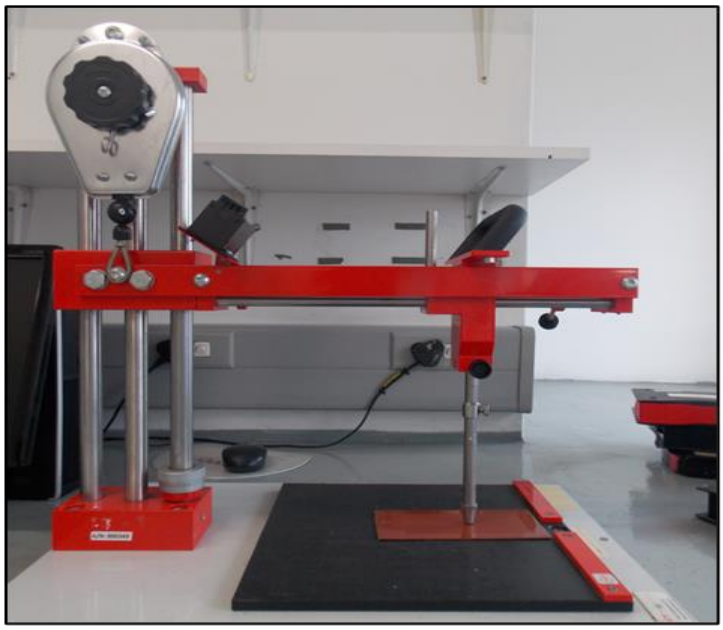

Figure 4:6. Scribe of the coating.

Exposure period and monitoring

The test samples were inspected at two-hour intervals, and the tested panels were gently rinsed with de-ionized water to remove any accumulated salt deposits. Following the rinse, the panels were immediately dried using a paper towel to avoid additional moisture exposure, which could alter the test outcomes. The panels were inspected for signs of corrosion and degradation. Once corrosion was initiated, the samples were further monitored to track the progression of damage for a minimum of 24 hrs.

Salt spray preparation

The salt spray was prepared in accordance with standard, ASTM B117 which specifies the parameters apparatus, procedures, and conditions (**Table 4.1**) necessary to generate and maintain the salt spray (fog) environment for corrosion testing.

During salt spray testing, samples are placed in an enclosed test chamber, constructed in compliance with ASTM B117 **(Figure 4:7)**. The samples are continuously exposed to an indirect spray of saltwater solution, commonly referred to as fog or mist.

The ASTM B117 salt spray test is a standardized method widely used to evaluate the corrosion resistance of materials and the adhesion performance of coatings. The corrosion severity was assessed visually (**Appendices 3-5**). Acceptable ratings depend on the application and customer requirements. This test is used to determine the durability under real-world conditions, helping manufacturers verify corrosion resistance and coating adhesion.

Table 4.1. Experimental parameters for ASTM B117.

Parameter	**Details**
Test Duration	Depending on the test material and application requirements.
Test Solution	5% salt solution (NaCl dissolved in de-ionised water), pH maintained between 6.5 and 7. 2.
Test Temperature	Maintained at 35°C ± 2°C.
Humidity	Maintained at 95% ± 5%.
Spray Rate	1.0 to 2.0 mL/hour per square meter of surface area, using pressurized air.
Specimen Preparation	Samples cleaned, dried, and prepared per test requirements before testing.
Corrosion Evaluation	Assessed visually or by measuring mass loss after the test period.

Figure 4:7. Illustration of the salt spray.

4.4.2) Artificial accelerated weathering preparation and testing

The test coated panel were mounted in the QUV and exposed to cycles of intense UV radiation followed by moisture exposure followed by condensation. These cycles were continued for five hundred hours.

MS was purchased from Q-Lab. Panels, with Type r-36 Matt finished steel panels made from cold-rolled MS with dimensions of (75 x 0.81 x 152) mm. The panels were degreased to remove surface contamination followed by clean water rinses. Samples of the WBA composites were adjusted to spray viscosity using water. These WBA composites were applied using a conventional air assisted spray gun, with nozzle orifice: 1.5 mm and nozzle pressure: 4.0bar.

The wet film thickness (WFT) of the coatings was 120 ±10 µm, measured with a wet film comb gauge from Elcometer, model number 3236. The coated samples were allowed to cure for six days at ambient temperature (23°C, 50% relative humidity) and

then further cured for one day in an oven at 54°C. The dry film thickness (DFT) was 15-45 µm, which was measured with a dry film Elcometer gauge, model number 456.

Accelerated weathering samples were measured on a Konica CM 3600 d spectrophotometer, and data were recorded using software, colibri 3.1.5 for comparison of the unexposed control samples and the exposed coating over time. The software was used to measure colour change degradation over various exposure times (40, 100, 200, 300, 400 and 500 hours).

Table 4.2. Parameters for QUV accelerated weathering conditions.

Parameter	**Details**
Test Duration	(40, 100, 200, 300, 400 and 500) hours
Test Solution	De-ionized waster
Condensation	50°C ± 5%.
UV exposure	70°C
Test Temperature	Maintained at 35°C ± 2°C
Humidity	Maintained at 95% ± 5%
Specimen Preparation	Samples cleaned, dried, and prepared per test requirements before testing.
QUV Evaluation	Assessed visually or by measuring mass loss after the test period Change in colour was measured on the Konica CM 3600D spectrophotometer, with software Colibri version 3.1.5

CHAPTER 5 – RESULTS AND DISCUSSION

This chapter entails the results and discussion of the performed study.

5.1) Characterization of anti-corrosiveness in the water-borne acrylic composites

The successful preparation of WBA composites, including $Zn_3(PO_4)_2$, WBA-GO, WBA-PVP, WBA-GO/PVP and WBA-$Zn_3(PO_4)_2$/PVP, was confirmed through various characterization techniques such as FTIR, XRD, FESEM, EDX and optical profilometry, as discussed below.

5.1.1) FTIR

FTIR spectroscopy was used to analyse the WBA composites. The FTIR spectrum of the WBA-nanomaterial composites shown in **Figure 5.1** revealed characteristic peaks corresponding to various functional groups **Table 5.1**, confirming the successful incorporation of the nanomaterial. A broad peak at ~3965 cm^{-1} was observed across all the samples, attributed to the O–H or N–H stretching, which is indicative of hydroxyl groups or hydrogen bonding. The presence of C=O stretching vibrations at ~1744–1750 cm^{-1}, prominent in WBA-GO and WBA-GO/PVP, highlighted the presence of carbonyl groups, whereas a peak at ~1617 cm^{-1}, corresponding to C=C stretching vibrations, confirmed the aromatic structure of graphene oxide. In the phosphate-containing samples, such as WBA-$Zn_3(PO_4)_2$ and WBA-$Zn_3(PO_4)_2$/PVP, intense peaks at ~1225–1285 cm^{-1} and ~1020–1032 cm^{-1} were attributed to P=O and P–O stretching vibrations, respectively, confirming the presence of phosphate groups. Additionally, the peak at 2378 cm^{-1}, was observed across all spectrums with varying intensities, corresponding to the atmospheric CO_2 absorption. **Figure 5.1(a) WBA-$Zn_3(PO_4)_2$** and **Figure 5.1(b) WBA-GO**, where similar, but there was peak intensity variations in **Figure 5.1(c) WBA-PVP**, **Figure 5.1(d) WBA-GO/PVP**, and **Figure 5.1(e) WBA-$Zn_3(PO_4)_2$/PVP**. The spectral shifts and peak broadening could indicate variations in functional group concentration, polymer interactions, or chemical modifications within the composites, affecting absorption behaviour of GO, PVP, and $Zn_3(PO_4)_2$ into the WBA matrix.

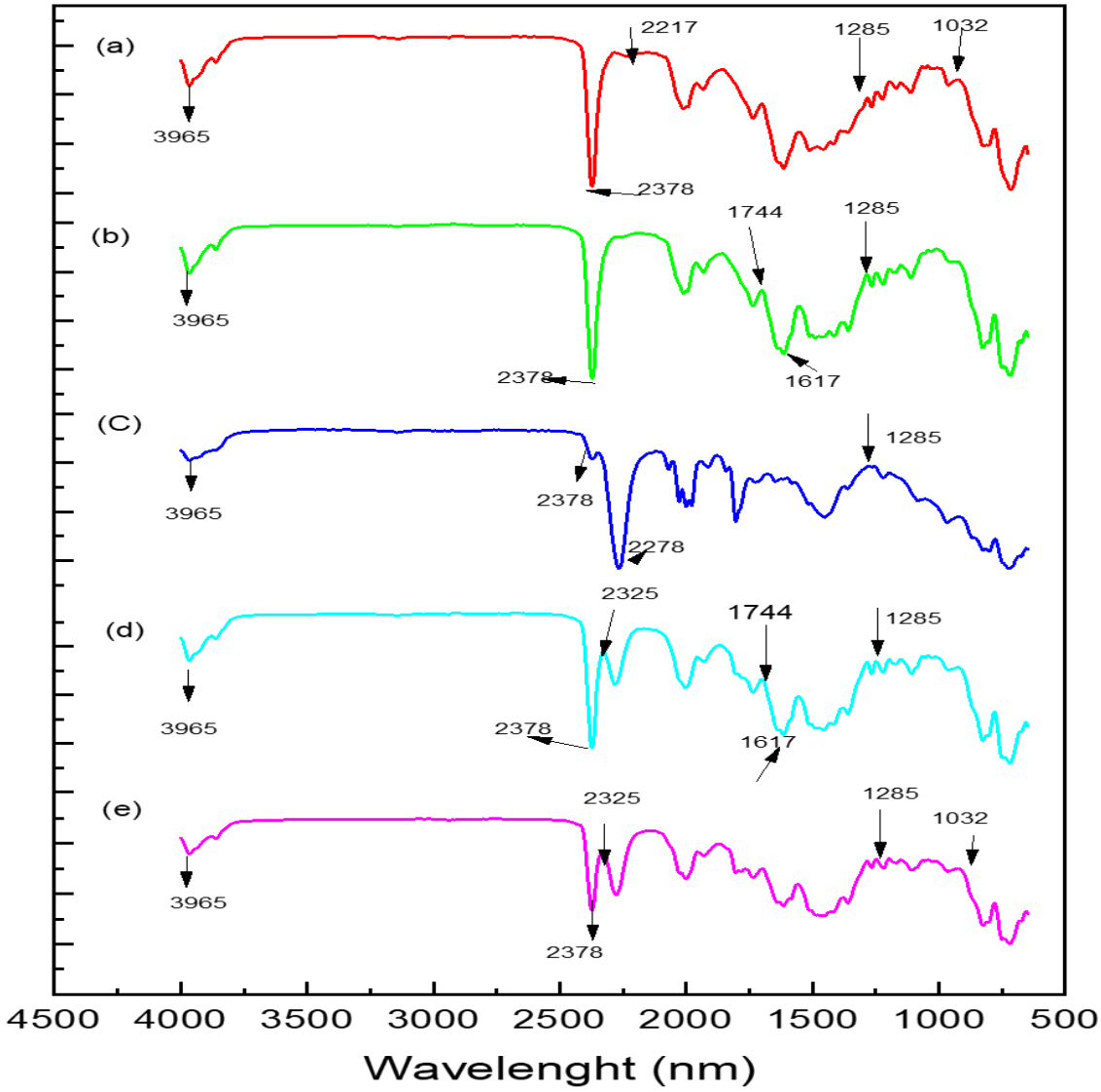

Figure 5:1. FTIR spectra of WBA-composites **(a)** WBA-$Zn_3(PO_4)_2$; **(b)** WBA-GO; **(c)** WBA-PVP; **(d)** WBA-GO/PVP and **(e)** WBA-$Zn_3(PO_4)_2$/PVP.

Table 5.1. FTIR peaks of the WBA nanomaterial composites (Silverstein, Webster and Kiemle 2005).

Average number range (cm^{-1})	Functional Group	Type of Vibration	Example Materials or Compounds
3400–3200	O–H (Hydrogen-bonded)	Stretch	Carboxylic acids, Alcohols
1750–1700	C=O (Carbonyl)	Stretch	Ketones, Aldehydes, Esters, GO
1700–1600	C=C (Aromatic, Alkene)	Stretch	Aromatic rings, Alkenes
1300–1000	C–O (Alcohol, Ester, Ether)	Stretch	Alcohols, Ethers, Esters, Polymers
1250–1020	P=O (Phosphate)	Stretch	Phosphates $Zn_3(PO_4)_2$

5.1.2) XRD

Figure 5.2 illustrates the diffraction patterns of various WBA composites, highlighting their distinct crystalline structures. The WBA-$Zn_3(PO_4)_2$ composite (**Figure 5.2a)** exhibits diffraction peaks at 2θ = 23.2°, 26°, 29°, 33°, and 35°, corresponding to the monoclinic crystalline structure of zinc phosphate, aligning with ICDD data (Ecco *et al.* 2016).

For WBA-GO **(Figure 5.2b),** characteristic peaks were observed at 10° and 26°. The peak at 10° corresponds to the (001) plane of GO, indicating oxygen-containing functional groups with an interlayer spacing of ~7.14 Å (JCPDS No. 75-1621), while the peak at ~26° corresponds to the (002) plane of reduced graphene oxide (rGO) with an interlayer distance of ~3.43 Å (JCPDS No. 75-2078) (Shalaby *et al.* 2015).

The WBA-PVP composite **(Figure 5.2c)** shows peaks within 20°–30°, consistent with the semi-crystalline nature of PVP, as reported in polymer crystallinity studies (A, Manohara and Gerward 2017).

For the WBA-GO/PVP composite **(Figure 5.2d)**, peaks were observed at ~10°, 26°, and 43°. The peak at ~10° (d ≈ 7.14 Å) corresponds to the (001) plane of GO, ~26° (d

≈ 3.43 Å) corresponds to the (002) plane of rGO, and the peak at ~43° (d ≈ 2.10 Å) is attributed to the (100) or (101) plane, indicating graphitic ordering (JCPDS No. 75-2078). Minor peaks within 20°–30° represent the semi-crystalline contribution of PVP (Chen et al., 2015).

Lastly, the WBA-$Zn_3(PO_4)_2$/PVP composite **(Figure 5.2e)** shows peaks at ~20°, 26°, 29°, 47°, and 56°. The peak at ~20° (d ≈ 4.44 Å) corresponds to the (200) plane and the peak at ~29° (d ≈ 3.07 Å) corresponds to the (120) plane of zinc phosphate (JCPDS No. 29-1458). Peaks at 47° and 56° represent higher-order planes of zinc phosphate, while the peak at ~26° suggests overlap between GO and PVP patterns, indicating residual contributions from both materials in the composite structure.

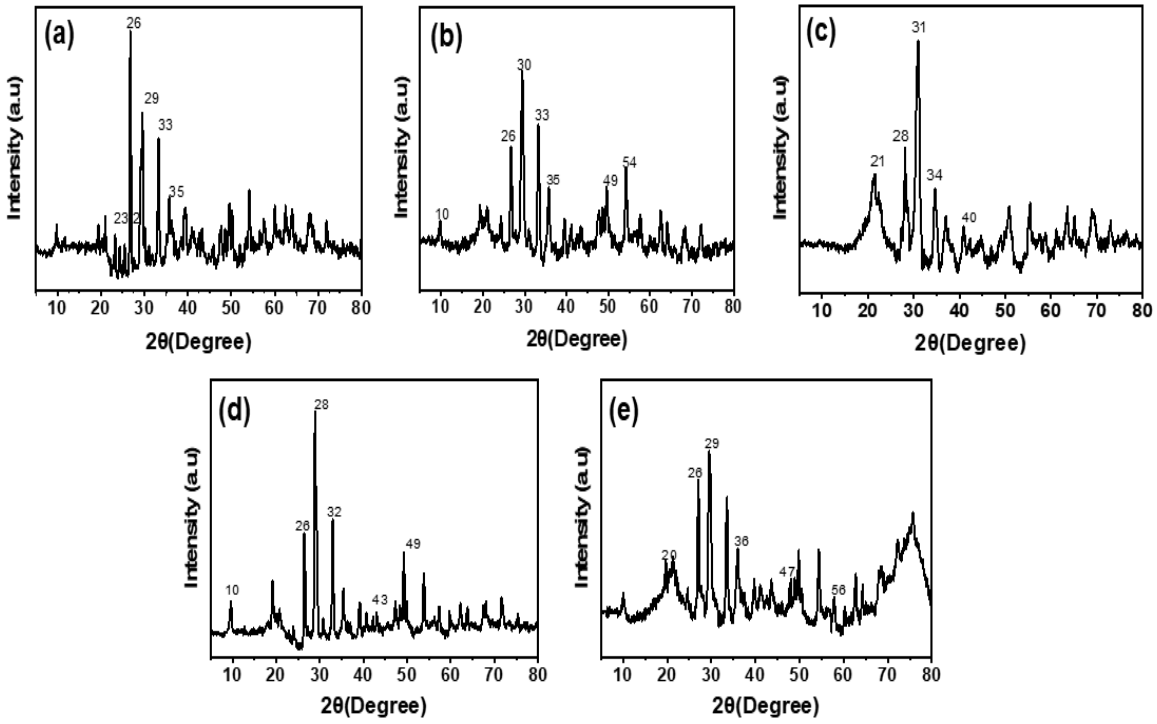

Figure 5:2. XRD analysis of (a) WBA-$Zn_3(PO_4)_2$; (b) WBA-GO; (c) WBA-PVP; (d) WBA-GO/PVP and (e) WBA-$Zn_3(PO_4)_2$/PVP.

5.2) Surface morphology and compositional studies

Corrosion resistance is a critical parameter for materials used in industrial applications, especially for metals exposed to aggressive environments. This study evaluated the performance of various WBA composite coatings applied to bare MS, FESEM, EDX, and optical profilometry **(Figures 5.3-5.5)**.

5.2.1) FESEM

The FESEM image of the bare metal surface (**Figure 5.3a**) reveals a rough topography characterized by irregularities and protrusions, which inherently enhance the adhesion of nanomaterial coatings by facilitating a stronger interfacial bond. In **Figure 5.3b**, the WBA-$Zn_3(PO_4)_2$ coating exhibits a significantly rougher and thicker surface, with the increased thickness contributing to its corrosion resistance properties. The WBA-GO coating (**Figure 5.3c**) displays a uniform and distinct morphology with visible graphene sheets, highlighting effective surface modification. The WBA-PVP coating (**Figure 5.3d**) reveals smooth and uniform coverage with minor irregularities. For composite coatings, the WBA-$Zn_3(PO_4)_2$/PVP system (**Figure 5.3f**) shows a smooth and uniform morphology, providing robust chemical and physical protection. In contrast, the WBA-PVP/GO composite coating (**Figure 5.3e**) exhibits a unique flake-like structure, indicative of synergistic interactions between PVP and GO, which enhance the coating's anti-corrosive properties.

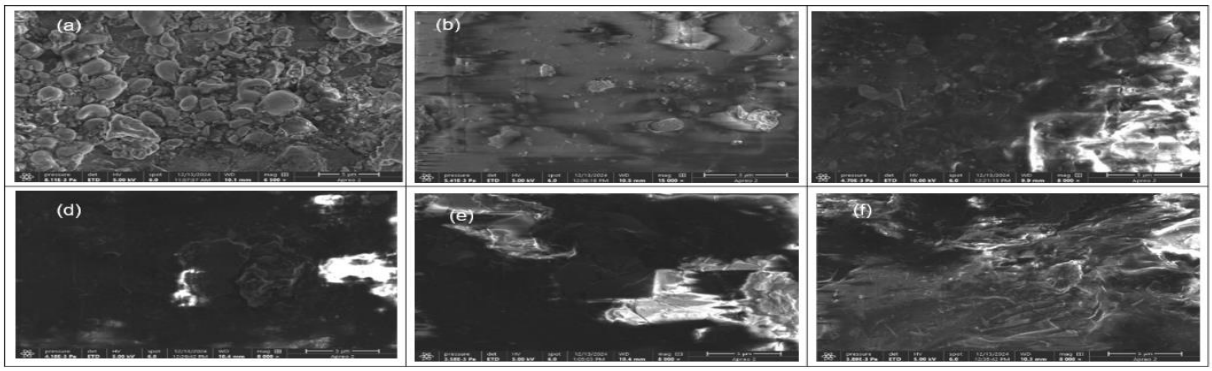

Figure 5:3. SEM micrographs showing the morphology of WBA composites (a) Bare-MS; (b) WBA-$Zn_3(PO_4)_2$; (c) WBA-GO; (d) WBA-PVP; (e) WBA-GO/ PVP and (f) WBA-$Zn_3(PO_4)_2$/ PVP.

5.2.2) EDX analysis

The corresponding EDX spectrum (**Figure 5.4a**) confirms the presence of iron (Fe) peaks, indicating the elemental composition of the untreated metal surface. The prominent presence of carbon in the EDX spectra **(Figures 5.4b–e),** aside from zinc, is attributed to the organic composition of the Water-borne acrylic composites, which includes the anti-corrosive nanomaterial. These carbon-based materials contribute significantly to the detected signal. Additionally, residual surfactants, dispersants, or environmental contaminants may further enhance carbon intensity. The use of carbon tape for sample mounting can also introduce extraneous carbon signals, especially in thin coatings. In contrast, **(Figure 5.4a),** bare mild steel predominantly shows Fe peaks, confirming the absence of these carbon-rich coatings. The variations in carbon intensity across **Figures 5.4b–e** suggest differences in coating composition, dispersion, and possible surface contamination.

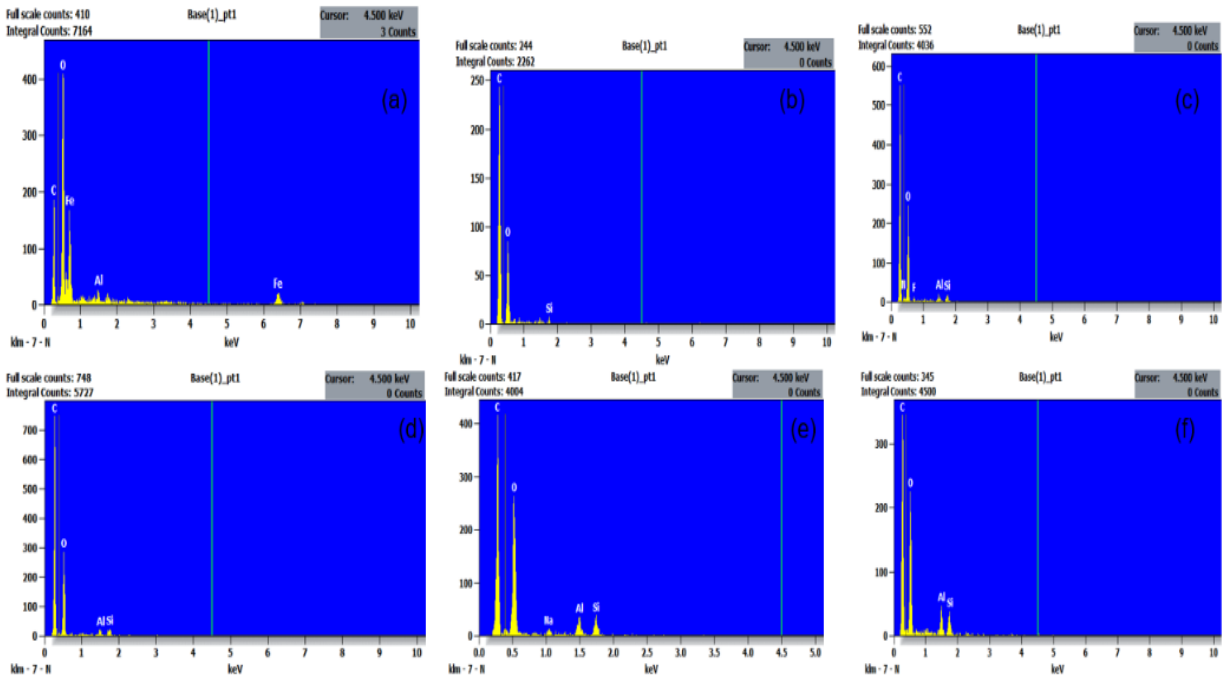

Figure 5:4. EDX spectra of WBA composites (a) Bare – MS; (b)WBA - Zn3(PO4)2; (c) WBA – GO; (d) WBA – PVP; (e) WBA - GO/ PVP and (f) WBA - $Zn_3(PO_4)_2$/ PVP

5.2.3) Optical Profilometer

Optical profilometry (**Figure 5.5**) further characterizes the roughness and topography for the bare and modified surfaces, represented in a 2-dimensional **(a-f)** and 3-

dimensional **(a''-f'')** perspectives, respectively. **Table 5.2.** FESEM Surface Roughness and Characteristics

Based on the FESEM, EDX, and optical profilometry results, the bare metal surface remains highly susceptible to severe corrosion due to the absence of any protective coating, with roughness values 27.03µm, characterized by notable irregularities.

Despite the high surface roughness values of WBA-$Zn_3(PO_4)_2$ (68.14µm) and WBA-GO (67.65µm), these coatings are the recommended choices based on salt spray testing and EIS results, which confirm their superior corrosion resistance. Although rough surfaces are often associated with increased susceptibility to corrosion, in this case, the roughness stems from the formation of protective layers rather than surface defects. WBA-$Zn_3(PO_4)_2$, creates a chemically stable phosphate barrier that reduces electrolyte penetration, while WBA-GO functions as an effective diffusion barrier, hindering ion transport despite its surface texture. Salt spray testing revealed that WBA-$Zn_3(PO_4)_2$ and WBA-GO coatings exhibited minimal corrosion product formation, indicating better long-term protection. EIS measurements further supported this, showing that these coatings had higher impedance values, signifying improved barrier properties.

In comparison WBA-PVP-containing coatings, WBA-GO/PVP (36.59µm) and WBA-$Zn_3(PO_4)_2$/PVP (54.44µm) (illustrated visible flake-like structures observed in FESEM), performed the worst in electrochemical tests despite appearing smooth in FESEM analysis. FESEM images showed a more uniform and compact structure for these coatings, initially suggesting better performance. However, electrochemical tests revealed higher corrosion current densities and lower polarization resistance, indicating reduced corrosion protection. The poor performance can be attributed to PVP's hydrophilic nature, which retains moisture and facilitates electrolyte penetration, accelerating corrosion processes.

This explains the discrepancy between FESEM observations and actual corrosion resistance, as FESEM only provides structural insights but does not account for electrochemical interactions or long-term stability. Therefore, despite the lower roughness values of WBA-PVP-containing coatings, the superior electrochemical

performance of WBA-$Zn_3(PO_4)_2$ and WBA-GO makes them the optimal choices for corrosion protection.

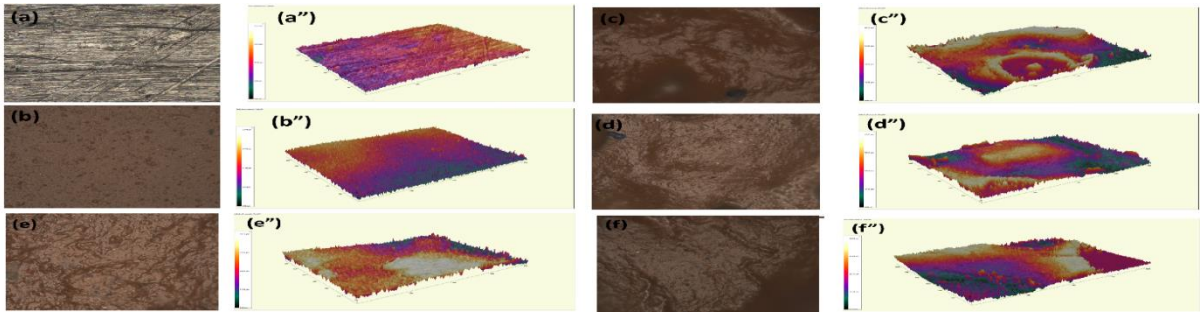

Figure 5:5. Two-and three-dimensional topography of the metal surface and the metal surface coated with WBA composites to measure roughness of the surface **(a) (a")** MS coated with **(b) (b")** WBA-$Zn_3(PO_4)_2$; **(c) (c")** WBA-GO; **(d) (d")** WBA-PVP; **(e) (e")** WBA-GO/ PVP and **(f) (f")** WBA-$Zn_3(PO_4)_2$/PVP.

Table 5.2. Surface roughness and morphological characteristics analysed by FESEM

Sample	Sample	Roughness (µm)	Surface Characteristics
a, a''	Bare Metal	27.03	Visible scratches, moderate roughness.
b, b"	WBA-$Zn_3(PO_4)_2$	68.14	Highest roughness due to thick phosphate layer.
c, c"	WBA-GO	67.65	Similar to WBA-$Zn_3(PO_4)_2$, but smoother and more uniform.
d, d"	WBA-PVP	49.79	Moderate roughness, improved surface modification.
e, e''	WBA-GO/PVP	36.59	Lowest roughness, uniform morphology.
f, f"	WBA-$Zn_3(PO_4)_2$/PVP	54.44	Moderate roughness with flake-like structures.

5.3) Electrochemical corrosion assessments

Corrosion protection properties of the water-borne acrylic composites using electrochemical methods.

5.3.1) Electrochemical impedance spectroscopy (EIS)

EIS was used to understand the frequency-dependent behaviour of an electrochemical system, providing data on the processes occurring at the working

electrode, such as charge transfer resistance (R_{ct}), double-layer capacitance (C_{dl}), and diffusion. Many authors use EIS data through Nyquist plots, bode modulus diagrams, and Bode phase angle diagrams, as each set of data provides some unique information on the system's impedance characteristics (Rivera-Grau *et al.* 2013; Umoren *et al.* 2015).

The EIS spectra of mild steel (MS) in 5% NaCl solution, with and without inhibitor-containing coatings at 25°C, are presented in **Figure 5.7**. The Nyquist plot in Figure 5.7(a) reveals arcs and semicircles that correspond to the R_{ct} and C_{dl} of the system. The semicircle diameter is a direct measure of R_{ct}, with larger diameters indicating greater corrosion resistance. Among the tested systems, WBA-$Zn_3(PO_4)_2$ exhibited the largest semicircle, with an R_{ct} value of 63.9 kΩ cm², signifying superior corrosion resistance. This performance is attributed to the passivation effect of $Zn_3(PO_4)_2$, which forms a protective layer that impedes charge transfer. In contrast, bare MS exhibited a significantly lower R_{ct} of 4.36 kΩ cm², demonstrating its susceptibility to corrosion.

WBA-GO displayed an intermediate semicircle diameter, indicating moderate barrier protection, defects in the GO film reduced its overall effectiveness. WBA-PVP, WBA-GO/PVP, and WBA-$Zn_3(PO_4)_2$/PVP demonstrated significantly smaller semicircles, indicative of lower R_{ct} values and poor inhibition efficiency. These findings suggest that the addition of PVP disrupts the passivation process, likely due to poor adhesion or weak interactions between the coating components.

The Bode phase angle diagram (**Figure 5.7c**) highlights the pseudocapacitive behaviour of the system, as the phase angles are below 90 degrees. A broader and higher peak in the phase angle corresponds to enhanced capacitive behaviour, indicative of a stable inhibitor layer and strong charge separation. The results align with observations from Nyquist and Bode modulus plots, with WBA-$Zn_3(PO_4)_2$ demonstrating the highest phase angle, followed by WBA-GO. The moderate performance of WBA-GO underscores its partial ability to block charge transfer, whereas the poor performance of PVP-containing systems suggests that PVP may compromise the integrity of the protective layer.

Equivalent circuit fitting was performed to model electrochemical interfaces and assess corrosion protection efficiency. The Randles circuit **(Figure 5.8)** was used to fit EIS

spectra, incorporating solution resistance (Rs), charge transfer resistance (Rct), and a constant phase element (CPE, Y_o). Statistical errors in the fitting parameters impact model accuracy, with low χ^2 values indicating reliable fits, while large uncertainties suggest deviations from ideal behaviour. The n values of the CPE reflect surface uniformity, with WBA-$Zn_3(PO_4)_2$ (n = 0.78) exhibiting near-ideal capacitive behaviour. WBA-GO/PVP and WBA-$Zn_3(PO_4)_2$/PVP had lower R_{ct} values and higher C_{dl}, suggesting weak passivation, which aligns with their negative inhibition efficiencies (-116.9% and -207.04%, respectively). These inconsistencies in surface film formation, particularly in WBA-PVP-based coatings, may be due to polymer swelling, poor adhesion, or increased water uptake.

The correlation between equivalent circuit parameters and electrochemical performance underscores the reliability of EIS modelling, as R_{ct} trends strongly align with η_{PDP} values. These results emphasize the need for optimizing composite formulations and improving material compatibility to enhance electrochemical stability and ensure long-term corrosion protection in harsh environments.

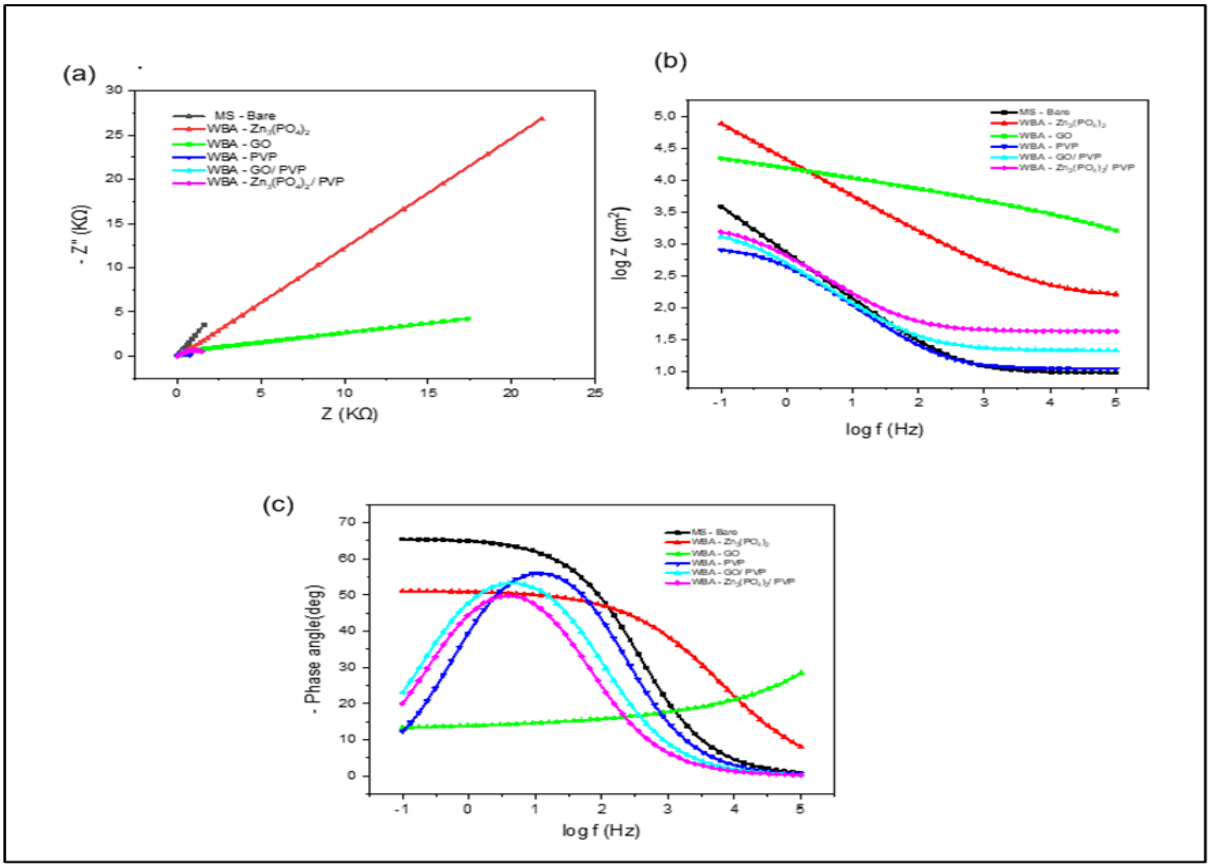

Figure 5:6. (a) Nyquist plots; **(b)** Bode plots and **(c)** phase angle plots for mild steel in 5% NaCl solution the absence and presence of different anti-corrosive nanomaterial.

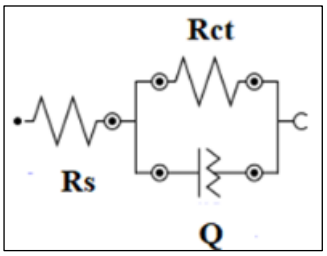

Figure 5:7. Randle's equivalent circuit for fitting of EIS spectra of MS in 5% NaCl.

Table 5.2 presents the parameters obtained on fitting of EIS spectra for the bare and coated MS. The n values are approaching 1, suggesting near ideal capacitive property of the electrodes (Quadri *et al.* 2017). The C_{dl} values were computed from Y_o and n values using **Eq. (3.5)**. A reduction in C_{dl} value noticed for WBA-$Zn_3(PO_4)_2$, could be attributed to its high inhibition property. An increase in inhibition efficiency (η_{eis}) is noticed with increase in R_{ct}, suggesting a direct relationship between the two variables. The results show excellent anticorrosive properties for WBA - $Zn_3(PO_4)_2$ and WBA–GO in comparison with the uncoated MS.

Table 5.2. EIS parameters for MS in 5% NaCl in the absence and presence of different anti-corrosive nanomaterials.

Inhibitor	**R_S ($K\Omega cm^{-2}$)**	**R_{ct} ($k\Omega cm^{-2}$)**	**n**	**Y_0 ($_(\mu\Omega sn\ cm^{-2}$)**	**C_{dl} ($_(\mu F\ cm^{-2}$)**	**η_{eis} (%)**
MS - Bare	9.24	4.36	0.752	289	3045.2	-
WBA - $Zn_3(PO_4)_2$	950	63.9	0.78	5.74	15.19	93.76
WBA - GO	2.38	14.5	0,722	173	3620.50	69.93
WBA - PVP	11	8.36	0.752	279	3595.36	47.84
WBA - GO/ PVP	20.9	2.01	0.704	311	4649.27	-116.9
WBA - $Zn_3(PO_4)_2$/ PVP	41.1	1.42	0.723	362	3873.82	-207.04

5.3.2) Open Circuit Potential (OCP) – Time profile, PDP and LPR studies

The Open Circuit Potential (OCP) measurements were used to assess the electrochemical stability of WBA-composites in a 5% saline environment. As shown in **Figure 5.6**, the OCP profiles display distinct stabilization trends, with each composite reaching a quasi-steady state at different potentials. The WBA-Blank exhibits the most negative potential (~ -0.68 V), indicating higher corrosion susceptibility. In contrast, WBA-$Zn_3(PO_4)_2$ and WBA-GO shift towards more noble potentials (~ -0.58 V), suggesting moderate protective behaviour through passivation.

OCP stabilization occurs between 600–1000 s, ensuring equilibrium before further electrochemical evaluations. The observed variations in OCP trends reflect differences in passivation, ion diffusion, and surface film integrity, directly influencing corrosion resistance.

WBA-$Zn_3(PO_4)_2$ demonstrate strong passivation, forming protective layers that minimize active corrosion. WBA-GO shows an initial increase in potential, suggesting ion exchange before stabilization, while WBA-Blank experiences a continuous decline, indicating persistent electrochemical activity and poor protection.

WBA-PVP, WBA-GO/PVP and WBA-$Zn_3(PO_4)_2$/PVP exhibit relatively stable OCP values, implying a barrier that reduces the rate of corrosion. Thus, WBA-$Zn_3(PO_4)_2$ and WBA-GO offer the best corrosion resistance, WBA-PVP, WBA-GO/PVP and WBA-$Zn_3(PO_4)_2$/PVP provide moderate barrier protection, and WBA-Bare remains the least effective due to continuous potential decline and active corrosion progression, indicating the effects of a uncoated panel as compared to the coated ms.

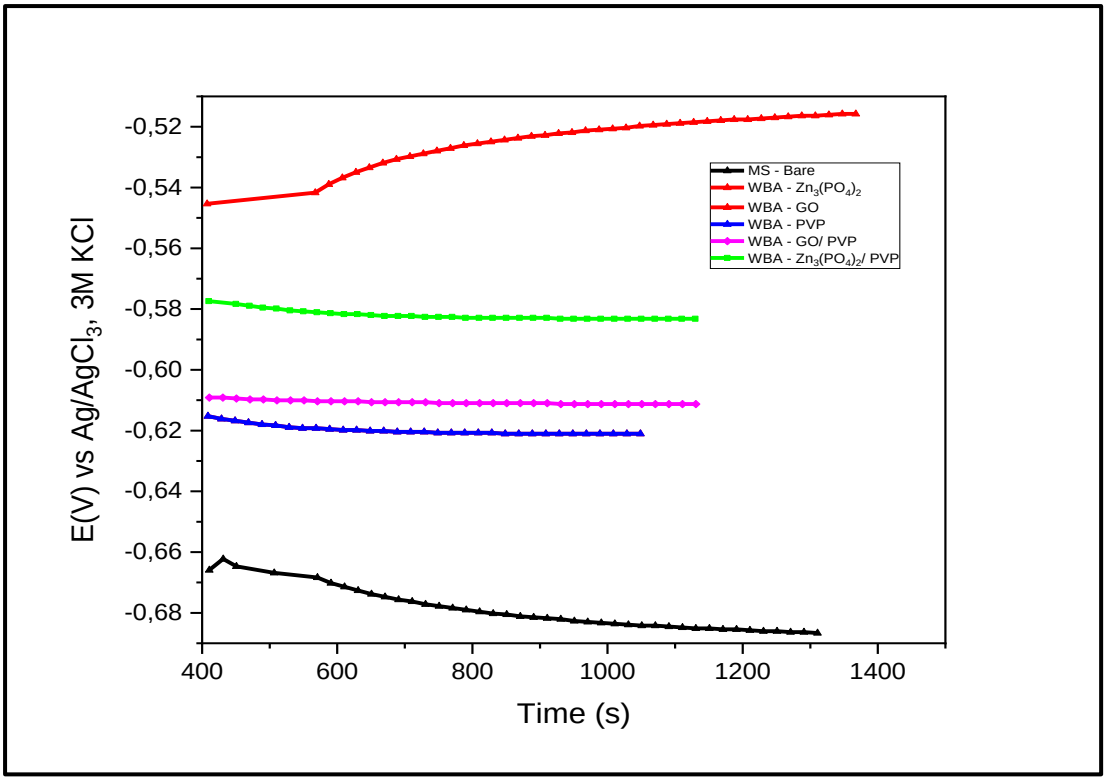

Figure 5:8. Variation of OCP with time on uncoated and coated WBA composites on MS in 5% saline solution.

5.3.3) Potentiodynamic polarization (PDP)

Figure 5.9 shows the Tafel polarization curves of MS in 5% H_2O at 25°C, revealing the electrochemical behaviour of different modified electrodes, in the absence and presence of the different anti-corrosive nanomaterials. These curves highlight the electrochemical performance, focusing on corrosion resistance and electrocatalytic activity, as reflected by variations in current density log_i against potential (V). The parameters for the electrochemical behaviour are reported in **Table 5.3**.

The anodic (βa) and cathodic (βC) Tafel slopes reveals the inhibition mechanisms of the different anti-corrosive coatings. The βa slope reflects the rate of metal dissolution, while βC indicates the rate of cathodic reduction reactions. A steeper βC suggests a system dominated by cathodic processes, whereas an increase in βa points to stronger anodic inhibition (Taiwo W. Quadri 2017).

For bare MS, βa = 60 mV/dec and βC = 267 mV/dec, suggesting a corrosion process formed by cathodic reactions, likely due to oxygen reduction and diffusion limitations (Biswal et al. 2021). The introduction of WBA-$Zn_3(PO_4)_2$ alters these kinetics significantly, increasing βa to 77 mV/dec while decreasing βC to 162 mV/dec. This trend suggests enhanced anodic inhibition through phosphate passivation, forming a protective layer that reduces metal dissolution and impedes charge transfer at the cathode (Yang et al. 2022).

WBA-GO exhibits a high βa of 119 mV/dec, indicating strong anodic inhibition, primarily via a barrier effect that limits metal oxidation. However, its high βC (269 mV/dec) remains close to that of bare MS, suggesting weak cathodic suppression and a less effective passivation mechanism compared to $Zn_3(PO_4)_2$ (Necolau and Pandele 2020).

The poor performance of PVP-containing coatings (WBA-PVP, WBA-GO/PVP, and WBA-$Zn_3(PO_4)_2$/PVP) is reflected in their lower βa (40–59 mV/dec) and βC (52–104 mV/dec) values, indicating poor barrier properties, increased permeability, and weak adhesion, which contribute to accelerated corrosion(Abdulhadi et al. 2023).

Shift in Corrosion Potential (E_{corr}) and Inhibition Mechanisms

Corrosion potential (E_{corr}) is another crucial parameter in determining the inhibition mechanism of a coating. An anodic shift in Ecorr suggests anodic inhibition, while a cathodic shift implies either poor anodic protection or increased cathodic reactivity (Zhang and Zhu 2021).

The uncoated MS-Bare sample produced a corrosion current density as (i_{corr} = 38) and a negative corrosion potential (-E_{corr} = 672). The absence of the surface modification caused the bare metal to be highly susceptible to oxidation and electrochemical degradation, as reflected by the steep slope and high current density at negative potentials.

WBA-GO (-E_{corr} = 504 mV) exhibits a significant anodic shift, confirming its role as an anodic inhibitor that effectively slows metal oxidation by forming a protective barrier. Similarly, WBA-$Zn_3(PO_4)_2$ (-E_{corr} = 668 mV) shows a slight anodic shift, indicating a

balanced inhibition mechanism where both anodic and cathodic reactions are suppressed through passivation. In contrast, WBA-PVP ($-E_{corr}$ = 705 mV), WBA-GO/PVP ($-E_{corr}$ = 701 mV), and WBA-$Zn_3(PO_4)_2$/PVP ($-E_{corr}$ = 653 mV) exhibit cathodic shifts, highlighting their inability to establish stable protective layers. This deficiency leads to increased corrosion susceptibility, as these coatings fail to hinder anodic dissolution and provide weak inhibition efficiency (Al Juhaiman, Mustafa and Mekhamer 2012; Camila and Alexandre 2014).

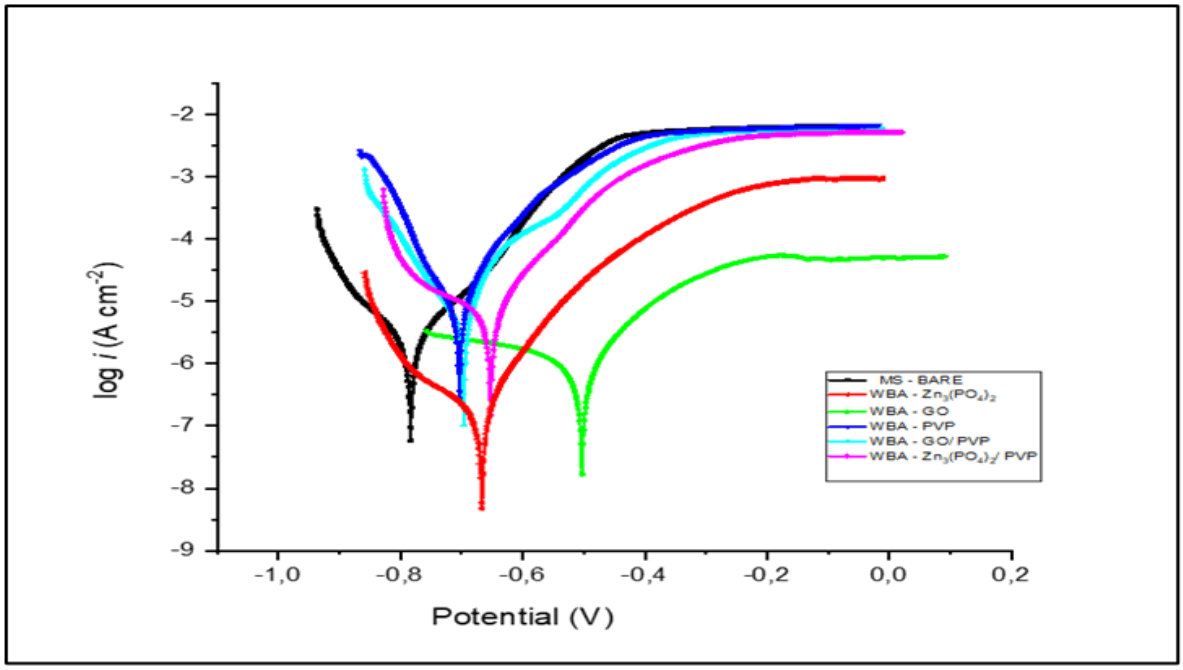

Figure 5:9. Tafel polarization curves of MS in 5% H_2O at 25°C of WBA composites.

Inhibitor	Type of Inhibition	PDP					LPR	
		$-E_{corr}$ (mv)	i_{corr} (μA/cm2)	βa (mV/dec)	βC (mV/dec)	η PDP (%)	R_P (Ω cm^2)	η_{LRP} (%)
MS- Bare		672	38	60	267		5588	-
WBA - Zn3(PO4)2	Passivation (Mixed Inhibition)	668	2	77	162	96	97477	94
WBA - GO	Anodic Inhibitor	504	8	119	269	79	30543	82

WBA - PVP	Poor Inhibition (Permeable & Weak Adhesion)	705	42	40	52	-10	1650	-239
WBA - GO/ PVP	Poor Inhibition (Weak Barrier Formation)	701	58	52	71	-53	1697	-229
WBA - Zn3(PO4)2/ PVP	Disrupted Passivation Effect	653	36	59	104	6	3061	-83

Table 5.3. Parameters obtained from the potentiodynamic and linear polarization curves of MS in 5% NaCl in the absence and presence of different anti-corrosive nanomaterials.

The values of Rp and the calculated η_{LPR} obtained from LPR measurements are also listed in **Table 5.3**. The results show that the Rp values for different anti-corrosive nanomaterials are greater than those of the blank solution. The low polarization resistance (RP= 5588 $\Omega\,cm^2$) of the bare metal confirms poor corrosion resistance, with no protective layer impeding the electrochemical processes. This reflects the effectiveness of the polymer nanocomposites in increasing the corrosion resistance of the studied metal in a 5% H_2O solution. There is good agreement between the η_{LPR} and η_{PDP} values. The PDP and LPR analyses highlight the effectiveness of $Zn_3(PO_4)_2$ based coatings, with WBA-$Zn_3(PO_4)_2$ emerging as the most promising material for corrosion inhibition. While WBA-GO provides moderate protection, the performance of composite systems (WBA-PVP, WBA-$Zn_3(PO_4)_2$/PVP and WBA-GO/PVP) indicates potential issues with material interactions or layer formation (Olasunkanmi, Sebona and Ebenso 2017).

5.4) Simulated environmental testing

5.4.1) Salt spray evaluation

The corroded surface areas of the WBA panels are shown in **Figures 5.10**-**5.11.** The cross- cut adhesion are illustrated in **Figures 5.12**. The related ratings of the corrosion creep, blister rating and blister frequency are summarized in **Table 5.4. Table 5.5** illustrates the cross- cut adhesion ratings of the coating to the MS panels. All MS surfaces coated with WBA composites clearly improved the corrosion resistance as compared the uncoated surface of the MS, which was heavily corroded. In accordance

with ASTM D1654, D714 and ASTM D3359 standard (**Appendices 3-4**), the performance of the coatings ranged from the worst to the best performers as follows:

MS- Bare < WBA–PVP< WBA-GO/ PVP < WBA-$Zn_3(PO_4)_2$/PVP < WBA-GO < WBA-$Zn_3(PO_4)_2$.

WBA-PVP, WBA-GO/PVP, WBA-$Zn_3(PO_4)_2$/PVP provided some protection against corrosion, but showed poor adhesion and poor blister resistance. WBA-$Zn_3(PO_4)_2$ demonstrated the best corrosion resistance, with minimal blistering and excellent adhesion.

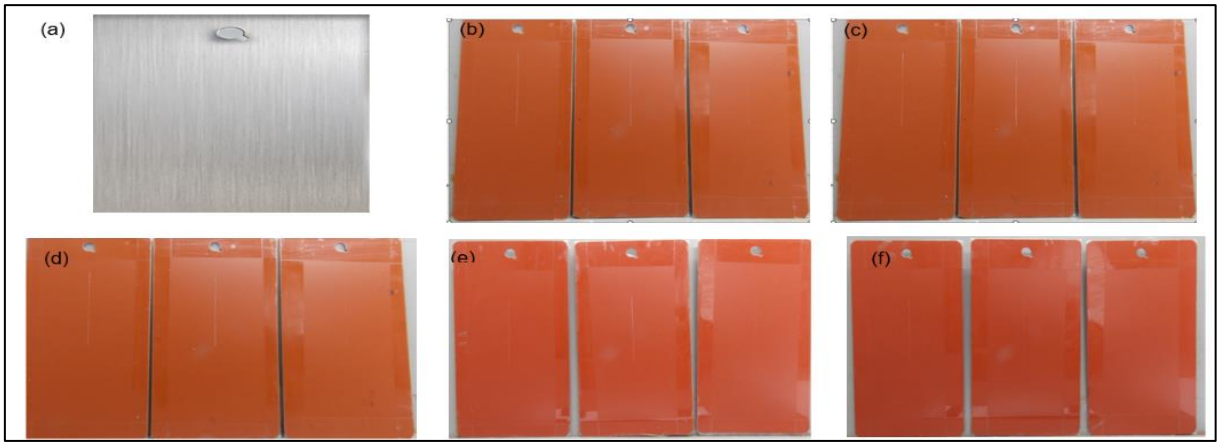

Figure 5:10. Uncoated and coated WBA composites on MS before exposure in a salt spray chamber **(a)** Bare – MS; **(b)** WBA - $Zn_3(PO_4)_2$; **(c)** WBA – GO; **(d)** WBA – PVP; **(e)** WBA - GO/ PVP and **(f)** WBA - $Zn_3(PO_4)_2$/ PVP.

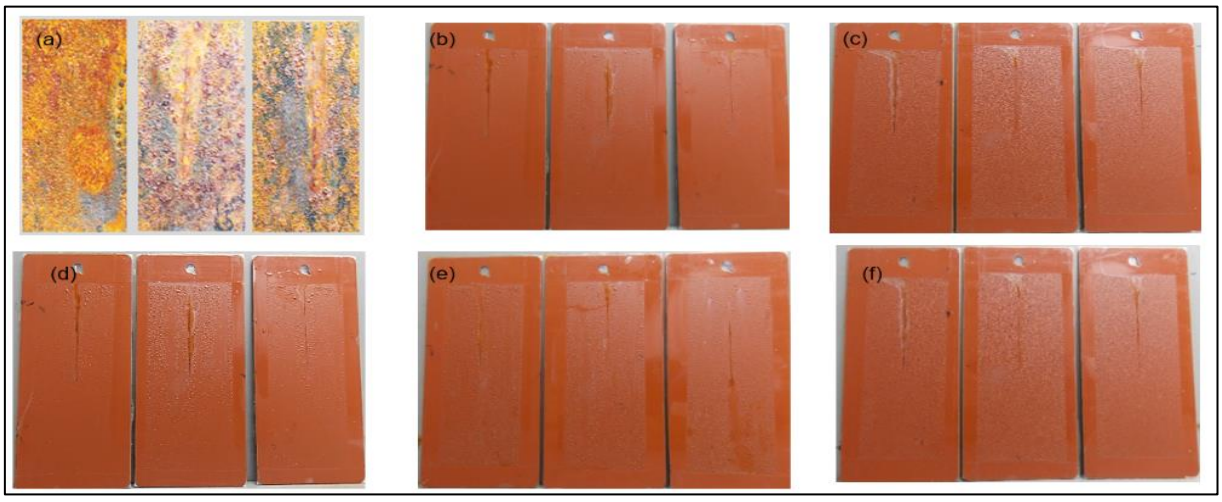

Figure 5:11. Uncoated and coated WBA composites on MS after 48 hrs exposure in a salt spray chamber **(a)** Bare – MS; **(b)** WBA - $Zn_3(PO_4)_2$; **(c)** WBA – GO; **(d)** WBA – PVP; **(e)** WBA - GO/ PVP and **(f)** WBA - $Zn_3(PO_4)_2$/ PVP.

Figure 5:12. Cross-cut adhesion test results on the ss exposure of WBA composites on MS **(a)** WBA-$Zn_3(PO_4)_2$; **(b)** WBA–GO; **(c)** WBA–PVP; **(d)** WBA-GO/PVP and **(e)** WBA- $Zn_3(PO_4)_2$/ PVP.

Table 5.4. Results evaluated based on corrosion resistance (ASTM D1654) and blistering (ASTM D714).

WBA-Nanocomposite	**Exposure Period (hrs)**	**ASTM D1654 (Corrosion creepage)**	**ASTM D714 (Blister Rating & Frequency)**
WBA - $Zn_3(PO_4)_2$	48	9 (Slight spread, <1 mm)	8 Medium
WBA - GO	48	7 (Visible corrosion, ~2 mm spread)	6 Medium
WBA - PVP	48	6 (Moderate corrosion, ~3 mm spread)	6 Dense
WBA - GO/ PVP	48	7 (Visible corrosion, ~2 mm spread)	7 Medium
WBA - $Zn_3(PO_4)_2$/ PVP	48	8 (Minimal corrosion, ~1 mm spread)	8 Medium

Table 5.5. Results evaluated in cross-cut adhesion (ASTM D3359) on the ss exposure of WBA composite coatings on MS.

WBA-Nanocomposite	**Exposure Period (hrs)**	**ASTM D3359 (Adhesion Rating)**
BA - $Zn_3(PO_4)_2$	48	4B (Minimal flaking)
WBA - GO	48	3B
WBA - PVP	48	3B
WBA - GO/ PVP	48	3B
WBA - $Zn_3(PO_4)_2$/ PVP	48	4B

5.5) Accelerated weather analysis

5.5.1) Accelerated QUV test results

The WBA coatings containing WBA-Zn3$(PO_4)_2$ and WBA-GO had the lowest increase in ΔE (change in colour), indicating better resistance to colour changes and improved stability under UV and moisture exposure (**Figures 5.13-5.15**). Compared with the WBA-Zn3$(PO_4)_2$ composite, the other WBA composites showed faster colour deterioration due to discolouration.

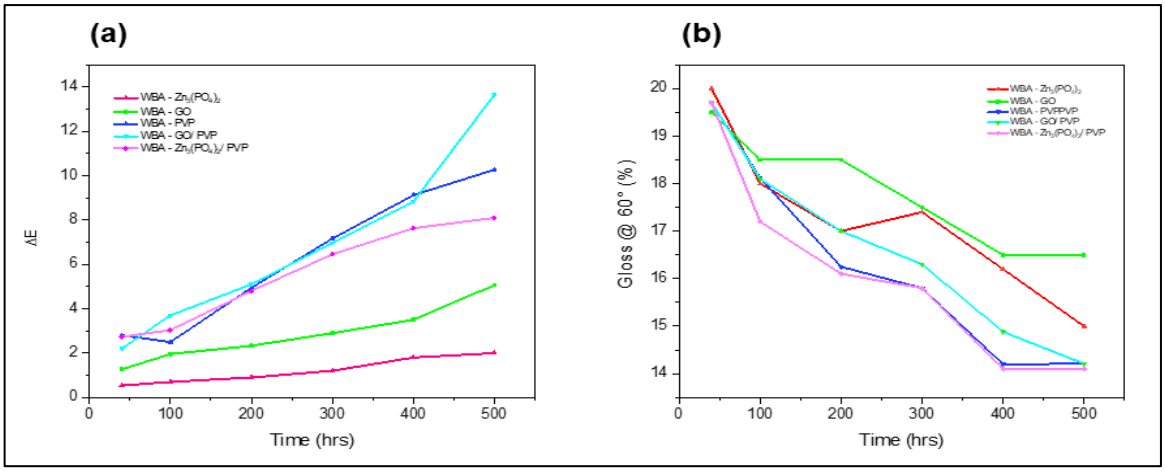

Figure 5:13. Coating of WBA with an anti-corrosive coating on MS for 500 hrs in a QUV accelerated weathering tester demonstrating **(a)** a change in colour and **(b)** a change in gloss.

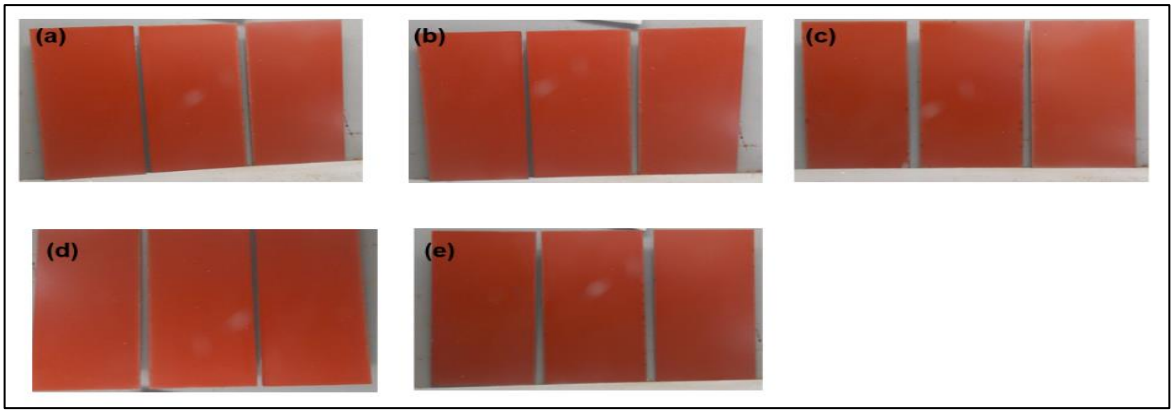

Figure 5:14. WBA composites before exposure to accelerated weather **(a)** WBA - $Zn_3(PO_4)_2$; **(b)** WBA – GO; **(c)** WBA – PVP; **(d)** WBA - GO/ PVP and **(e)** WBA - $Zn_3(PO_4)_2$/ PVP.

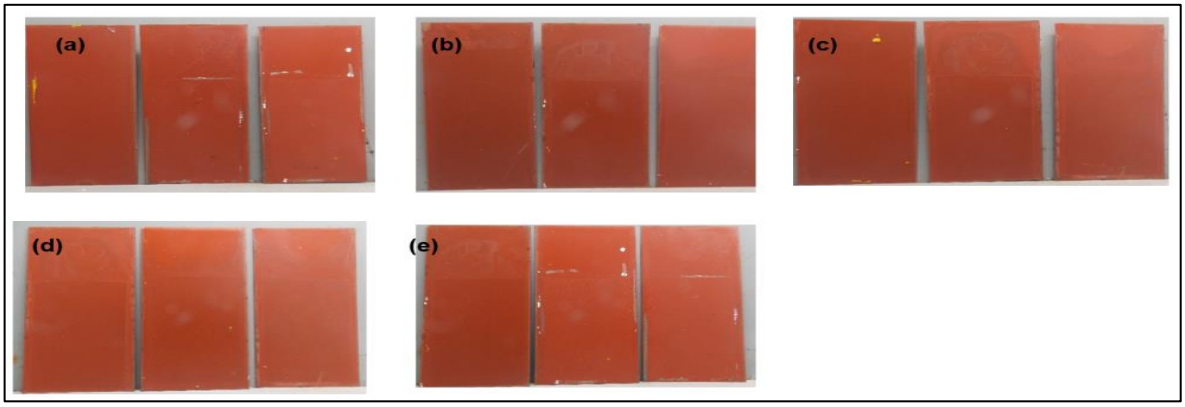

Figure 5:15. WBA composites after 500 hrs exposure to accelerated weather **(a)** WBA - $Zn_3(PO_4)_2$; **(b)** WBA – GO; **(c)** WBA – PVP; **(d)** WBA - GO/ PVP and **(e)** WBA - $Zn_3(PO_4)_2$/ PVP.

CHAPTER 6 – CONCLUSION AND FUTURE RECOMMENDATIONS

Provides a summary of the conclusions and recommendations of this work.

6.1) Conclusions

This study confirms that Water-borne acrylic (WBA) anti-corrosive nanocoating, significantly improve the corrosion resistance of mild steel in aggressive saline environments. FTIR and XRD analysis validated the incorporation of nanomaterials, with phosphate and graphene oxide interactions enhancing structural integrity.

Characterization using FTIR and XRD validated the incorporation of nanomaterials such as zinc phosphate ($Zn_3(PO_4)_2$) and graphene oxide (GO) into the WBA matrix. FTIR analysis identified key functional groups like P=O and C=C, which are indicative of phosphate and graphene oxide interactions. XRD confirmed the crystalline structures of WBA-$Zn_3(PO_4)_2$ and WBA-GO.

FESEM images showed that WBA-$Zn_3(PO_4)_2$ formed a dense, uniform layer, while WBA-GO displayed a layered morphology, contributing to corrosion resistance. EDX confirmed Zn and P peaks in WBA-$Zn_3(PO_4)_2$, supporting its passivation mechanism, while optical profilometry highlighted its smoother surface compared to PVP-containing coatings.

Electrochemical tests revealed WBA-$Zn_3(PO_4)_2$ as the most effective inhibitor, with an R_{ct} of 63.9 kΩ·cm², η_{EIS} of 93.76%, and i_{corr} of 2 µA/cm², confirming its superior passivation. WBA-GO provided moderate protection (R_{ct}: 14.5 kΩ·cm², η_{EIS}: 69.93%). In contrast, PVP-based coatings exhibited weak adhesion and higher corrosion rates, with decreasing inhibition efficiencies (47.84 to -207.04%).

Salt spray and QUV tests further confirmed WBA-$Zn_3(PO_4)_2$'s durability, with minimal corrosion (4B adhesion rating, ΔE = 9).

These findings highlight that WBA-$Zn_3(PO_4)_2$ and WBA-GO as promising, environmentally friendly anti-corrosive coatings. The results suggest that these Water-borne acrylic nanocomposites, with their low VOC content, present a sustainable and effective solution for corrosion protection in challenging environments.

6.2) Future recommendations

6.2.1 Optimization of Hydrophobicity and Adhesion

Incorporation of more hydrophobic anti-corrosive nanomaterial, or adhesion-promoting additives, in a coatings formulation should be investigated, to enhance the coating properties and reduce permeability. This could improve corrosion resistance by limiting water ingress.

6.2.2 Alternative Anti-Corrosive Additives

Investigating alternative additives such as cerium salts or zinc molybdate, as potential replacements, could enhance corrosion resistance and mitigate issues related to passivation disruption in PVP-containing systems.

6.2.3 Large-Scale Industrial Application of Graphene Oxide

Graphene oxide (GO) remains a promising candidate for corrosion-resistant coatings. While WBA-GO exhibited moderate corrosion resistance, industrial-grade GO should be tested to determine its performance consistency on a larger scale. Further studies should focus on optimizing its dispersion and compatibility with acrylic resins. Additionally, research should focus on optimizing the protective properties of graphene oxide (GO)-based coatings, by exploring alternative Water-borne acrylic resin or surfactants that can improve compatibility and adhesion within GO layers. This modification could address existing defects and significantly enhance the barrier performance of these coatings.

REFERENCES

A, S., Manohara, S. R. and Gerward, L. 2017. Influence of polyvinylpyrrolidone on optical, electrical, and dielectric properties of poly(2-ethyl-2-oxazoline)-polyvinylpyrrolidone blends. *Journal of Molecular Liquids*, 247: 328-336.

Abdulhadi, S., Mohammed, A., Al-Azzawi, W. K., Gaaz, T., Kadhum, A. A. H., Shaker, L. M. and Al-Amiery, A. A. 2023. The corrosion inhibition abilities of PVA and PVP against the corrosion of mild steel in hydrochloric acid. *International Journal of Corrosion and Scale Inhibition*, 12: 645–663

Akpan, E. D., Oladipo, S. D., Quadri, T. W., Olasunkanmi, L. O., Nwanna, E. E., Omondi, B. and Ebenso, E. E. 2022. Formamidine-Based Thiuram Disulfides as Efficient Inhibitors of Acid Corrosion of Mild Steel: Electrochemical, Surface, and Density Functional Theory/Monte Carlo Simulation Studies. *ACS Omega*, 7 (30): 26076-26091.

Al Juhaiman, L. A., Mustafa, A. A. and Mekhamer, W. K. 2012. Polyvinyl Pyrrolidone as a Green Corrosion Inhibitor of Carbon Steel in Neutral Solutions Containing NaCl: Electrochemical and Thermodynamic Study. *International Journal of Electrochemical Science*, 7 (9): 8578-8596.

Ali Salman, A. 2020. Application of Nanomaterials in Environmental Improvement. In: Mousumi, S. ed. *Nanotechnology and the Environment*. Rijeka: IntechOpen, Ch. 2. Available: https://doi.org/10.5772/intechopen.91438 (Accessed 2024-12-11).

Allen, L. J., D'Alfonso, A. J., Freitag, B. and Klenov, D. O. 2012. Chemical mapping at atomic resolution using energy-dispersive x-ray spectroscopy. *MRS Bulletin*, 37 (1): 47-52.

An, H., Liu, K., Wang, S., Jiang, C., Liang, S., Xiao, J., Zhao, X., Sun, Z., Cao, C. and Gao, Y. 2023. Enhanced Corrosion Resistance of Waterborne Epoxy Coatings by Polyaniline Nanorods and Nitrogen and Fluorine Dual-Doped Graphene Oxide Composites. *ACS Applied Nano Materials*, 6 (14): 13250-13259.

B. del Amo, R. Romagnoli, C. Deyá and González, J. A. 2002. High performance water-based paints with non-toxic anticorrosive pigments. *Progress in Organic Coatings* 45: 389–397.

Barroso, M. M. 2014. Formulation of anticorrosive paints employing conducting polymers. Article IDUniversitat Politècnica de Catalunya.

Berthomieu, C. and Hienerwadel, R. 2009. Fourier transform infrared (FTIR) spectroscopy. *Photosynthesis Research*, 101 (2): 157-170.

Bierwagen, G. P. 1998. Corrosion and Its Control by Coatings. In: *Organic Coatings for Corrosion Control*. American Chemical Society, 1-8. Available: https://doi.org/10.1021/bk-1998-0689.ch001 (Accessed 2024/12/11).

Biswal, J., Pant, H. J., Sharma, V. K., Sharma, S. C. and Gupta, A. K. 2021. Evaluation of inhibition effect of poly vinyl pyrrolidone on corrosion of bronze in simulated acid rain using thin layer activation technique. *Nuclear Instruments and Methods in Physics Research Section B: Beam Interactions with Materials and Atoms*, 503: 30-36.

Boumhara, K., Harhar, H., Tabyaoui, M., Bellaouchou, A., Guenbour, A. and Zarrouk, A. 2018. Corrosion Inhibition of Mild Steel in 0.5 M H2SO4 Solution by Artemisia herba-alba Oil. *Journal of Bio- and Tribo-Corrosion*, 5 (1): 8.

Bunch, J. S., Verbridge, S. S., Alden, J. S., van der Zande, A. M., Parpia, J. M., Craighead, H. G. and McEuen, P. L. 2008. Impermeable Atomic Membranes from Graphene Sheets. *Nano Letters*, 8 (8): 2458-2462.

Callister Jr, W. D. and Rethwisch, D. G. 2020. *Materials Science and Engineering: An Introduction*. John Wiley & Sons.

Camila, G. D. and Alexandre, F. G. 2014. Corrosion Inhibitors – Principles, Mechanisms and Applications. In: Aliofkhazraei, M. ed. *Developments in Corrosion Protection*. Rijeka: IntechOpen, Ch. 16. Available: https://doi.org/10.5772/57255 (Accessed 2024-12-11).

Chen, W., Shi, H., Liu, W., Zhao, A., Pan, G., Huang, A., Yu, Y. and Ma, L. 2023. Study on the Preparation and Corrosion Resistance Properties of Superhydrophobic Coatings on Galvanized Steel. *Metals*, 13 (2): 260.

Chimenti, S. V., Jesús & García-Lecina, E. & Grande, Hans-Jurgen & Paulis, María & Leiza, Jose. 2019. Combined Effect of Crystalline Nanodomains and in Situ Phosphatization on the Anticorrosion Properties of Waterborne Composite Latex Films. *Industrial & Engineering Chemistry Research. 58. 10.1021/acs.iecr.9b02233.* , 58 (46): 1-9.

Dallaire, S., Dufour, M. and Gauthier, B. 1993. Characterization of wear damage in coatings by optical profilometry. *Journal of Thermal Spray Technology*, 2: 363-368.

Ecco, L. G., Fedel, M., Deflorian, F., Becker, J., Iversen, B. B. and Mamakhel, A. 2016. Waterborne acrylic paint system based on nanoceria for corrosion protection of steel. *Progress in Organic Coatings*, 96: 19-25.

Epp, J. 2016. 4 - X-ray diffraction (XRD) techniques for materials characterization. In: Hübschen, G., Altpeter, I., Tschuncky, R. and Herrmann, H.-G. eds. *Materials Characterization Using Nondestructive Evaluation (NDE) Methods*. Woodhead Publishing, 81-124. Available: https://www.sciencedirect.com/science/article/pii/B9780081000403000043 (Accessed

Gao, F., Luo, Y., Xu, J., Du, X., Wang, H., Cheng, X. and Du, Z. 2021a. Preparation of graphene oxide-based polyaniline composites with synergistic anticorrosion effect for waterborne polyurethane anticorrosive coatings. *Progress in Organic Coatings* 156: 1-11.

Gao, F., Mu, J., Bi, Z., Wang, S. and Li, Z. 2021b. Recent advances of polyaniline composites in anticorrosive coatings: A review. *Progress in Organic Coatings*, 151: 106071.

Gimeno L, R. M., & Laguna, O. 2014. Development of Second-Generation Zinc Phosphate Pigments for Enhanced Corrosion Protection. *Surface Coatings International,*, 87 (3): 189-197.

Gimeno, M. J., Puig, M., Chamorro, S., Molina, J., March, R., Oró, E., Pérez, P., Gracenea, J. J. and Suay, J. J. 2016. Improvement of the anticorrosive properties of an alkyd coating with zinc phosphate pigments assessed by NSS and ACET. *Progress in Organic Coatings*, 95: 46-53.

Hare, C. H. 1995. Protective Coatings: Fundamentals of Chemistry and Composition. *Surface Coatings International*, 78 (4): 157-165.

Hunger, K. and Schmidt, M. U. 2019. *Industrial Organic Pigments: Production, Crystal Structures, Properties, Applications*. John Wiley & Sons.

Ijsseling, F. P. 1989. General guidelines for corrosion testing of materials for marine applications: Literature review on sea water as test environment. *British Corrosion Journal*, 24 (1): 53-78.

Indu, Yadav, A., Mandal, M. K. and Dubey, K. K. 2020. Nanomaterial Biosynthesis and Enzyme Immobilization. In: *Green Synthesis of Nanomaterials for Bioenergy Applications*. 191-209. Available: https://onlinelibrary.wiley.com/doi/abs/10.1002/9781119576785.ch8 (Accessed

Information, N. C. f. B. 2024. Zinc phosphate. *PubChem*, Article ID.

John, S., Kuruvilla, M. and Joseph, A. 2013. Surface morphological and impedance spectroscopic studies on the interaction of polyethylene glycol (PEG) and polyvinyl pyrrolidone (PVP) with mild steel in acid solutions. *Research on Chemical Intermediates*, 39 (3): 1169-1182.

Kelly, B. M. 2017. Electrochemical Method for Characterization and Ranking of Corrosion Inhibitors. Article IDNorth Dakota State University.

Knudsen, O. Ø. and Forsgren, A. 2017. *Corrosion Control Through Organic Coatings (2nd ed.)*. CRC press.

Lei, Y., Qiu, Z., Tan, N., Du, H., Li, D., Liu, J., Liu, T., Zhang, W. and Chang, X. 2020. Polyaniline/CeO2 nanocomposites as corrosion inhibitors for improving the corrosive performance of epoxy coating on carbon steel in 3.5% NaCl solution. *Progress in Organic Coatings*, 139: 105430.

Lewczuk, B. and Szyryńska, N. 2021. Field-Emission Scanning Electron Microscope as a Tool for Large-Area and Large-Volume Ultrastructural Studies. *Animals*, 11 (12): 3390.

Liu, Z., Zhang, B., Yu, H., Zhang, Z., Jiang, W. and Ma, Z. 2022. A Smart Anticorrosive Epoxy Coating Based on Graphene Oxide/Functional Mesoporous Silica Nanoparticles for Controlled Release of Corrosion Inhibitors. *Coatings*, 12 (11): 1749.

Low, E. J., Yusoff, H. M., Batar, N., Nor Azmi, I. N. Z., Chia, P. W., Lam, S. S., Kan, S.-Y., Liew, R. K., Lee, G. E., Venkateswarlu, K. and Ridwan Zulkifli, M. F. 2023. The use of food additives as green and environmental-friendly anti-corrosion inhibitors for protection of metals and alloys: a review. *Environmental Science and Pollution Research*, 30 (31): 76297-76307.

Lyon, S. B., Bingham, R. and Mills, D. J. 2017. Advances in corrosion protection by organic coatings: What we know and what we would like to know. *Progress in Organic Coatings*, 102: 2-7.

Magar, H. S., Hassan, R. Y. A. and Mulchandani, A. 2021. Electrochemical Impedance Spectroscopy (EIS): Principles, Construction, and Biosensing Applications. *Sensors*, 21 (19): 6578.

Maile, F. J., Pfaff, G. and Reynders, P. 2005. Effect pigments—past, present and future. *Progress in Organic Coatings*, 54 (3): 150-163.

Mariz, I. d. F. A., Millichamp, I. S., de la Cal, J. C. and Leiza, J. R. 2010. High performance water-borne paints with high volume solids based on bimodal latexes. *Progress in Organic Coatings*, 68 (3): 225-233.

Mekuye, B. and Abera, B. 2023. Nanomaterials: An overview of synthesis, classification, characterization, and applications. *Nano Select*, 4 (8): 486-501.

Mishra, A., Aslam, J., Verma, C., Quraishi, M. A. and Ebenso, E. E. 2020. Imidazoles as highly effective heterocyclic corrosion inhibitors for metals and alloys in aqueous electrolytes: A review. *Journal of the Taiwan Institute of Chemical Engineers*, 114: 341-358.

Mobin, M. and Shabnam, H. 2010. Corrosion Behavior of Mild Steel and SS 304L in Presence of Dissolved Copper. *Journal of Minerals and Materials Characterization and Engineering*, 9 (12): 18.

Necolau, M.-I. and Pandele, A.-M. 2020. Recent Advances in Graphene Oxide-Based Anticorrosive Coatings: An Overview. *Coatings*, 10 (12): 1149.

Olasunkanmi, L. O., Sebona, M. F. and Ebenso, E. E. 2017. Influence of 6-phenyl-3 (2H)-pyridazinone and 3-chloro-6-phenylpyrazine on mild steel corrosion in 0.5 M HCl medium: experimental and theoretical studies. *Journal of Molecular Structure*, 1149: 549-559.

Parhizkar, N., Ramezanzadeh, B. and Shahrabi, T. 2018. Corrosion protection and adhesion properties of the epoxy coating applied on the steel substrate pre-treated by a sol-gel based silane coating filled with amino and isocyanate silane functionalized graphene oxide nanosheets. *Applied Surface Science*, 439: 45-59.

Pikaar, I., Sharma, K. R., Hu, S., Gernjak, W., Keller, J. and Yuan, Z. 2014. Reducing sewer corrosion through integrated urban water management. *Science*, 345 (6198): 812-814.

Pourhashem, S., Saba, F., Duan, J., Rashidi, A., Guan, F., Nezhad, E. G. and Hou, B. 2020. Polymer/Inorganic nanocomposite coatings with superior corrosion protection performance: A review. *Journal of Industrial and Engineering Chemistry*, 88: 29-57.

Q-lab. 2024. QUV Accelerated Weathering Tester. *Q-lab*, 1 (1): 17.

Quadri, T. W., Olasunkanmi, L. O., Fayemi, O. E., Solomon, M. M. and Ebenso, E. E. 2017. Zinc oxide nanocomposites of selected polymers: synthesis, characterization, and corrosion inhibition studies on mild steel in HCl solution. *ACS omega*, 2 (11): 8421-8437.

Rabek, J. F. 2012. *Polymer Photodegradation: Mechanisms and Experimental Methods*. Springer Science & Business Media.

Raistrick, I. D. 1986. Application of Impedance Spectroscopy to Materials Science. *Annual Review of Materials Research*, 16 (Volume 16): 343-370.

Ramoškienė, E., Gladkovas, M. and Šalkauskas, M. 2003. Validation of salt spray corrosion test. *Accreditation and Quality Assurance*, 8 (5): 235-241.

Randviir, E. P. and Banks, C. E. 2013. Electrochemical impedance spectroscopy: an overview of bioanalytical applications. *Analytical Methods*, 5 (5): 1098-1115.

Ress, J., Martin, U. and Bastidas, D. M. 2021. Improved Corrosion Protection of Acrylic Waterborne Coating by Doping with Microencapsulated Corrosion Inhibitors. *Coatings*, 11 (9): 1134.

Revie, R. W. and Uhlig, H. H. 2008. Definition and Importance of Corrosion. In: *Corrosion and Corrosion Control*. 1-8. Available: https://doi.org/10.1002/9780470277270.ch1 (Accessed 2024/12/11).

Rivera-Grau, L. M., Casales, M., Regla, I., Ortega-Toledo, D. M., Ascencio-Gutierrez, J. A., Porcayo-Calderon, J. and Martinez-Gomez, L. 2013. Effect of Organic Corrosion Inhibitors on the Corrosion Performance of 1018 Carbon Steel in 3% NaCl Solution. *International Journal of Electrochemical Science*, 8 (2): 2491-2503.

Rouya, E., Cattarin, S., Reed, M. L., Kelly, R. G. and Zangari, G. 2012. Electrochemical Characterization of the Surface Area of Nanoporous Gold Films. *Journal of The Electrochemical Society*, 159 (4): K97.

Saji, V. S. 2012. 1 - The impact of nanotechnology on reducing corrosion cost. In: Saji, V. S. and Cook, R. eds. *Corrosion Protection and Control Using Nanomaterials*. Woodhead Publishing, 3-15. Available: https://www.sciencedirect.com/science/article/pii/B9781845699499500010 (Accessed

Sam John, M. K., Abraham Joseph. 2012. Surface morphological and impedance spectroscopic studies on the interaction of polyethylene glycol (PEG) and polyvinyl pyrrolidone (PVP) with mild steel in acid solutions. *Springer Science*, 10.1007/s11164-012-0675-x: 39:1169–1118.

Shalaby, A., Nihtianova, D., Markov, P., Staneva, A., Iordanova, R. and Dimitriev, Y. 2015. Structural analysis of reduced graphene oxide by transmission electron microscopy. *Bulgarian Chemical Communications*, 47 (1): 291-295.

Shumaila, M., Anujit, G., Eram, S., Fahmina, Z. and Nahid, N. 2022. Introductory Chapter: Corrosion. In: Fahmina, Z., Anujit, G. and Eram, S. eds. *Corrosion*. Rijeka: IntechOpen, Ch. 1. Available: https://doi.org/10.5772/intechopen.103791 (Accessed 2024-12-11).

Sillanpää, M. and Shestakova, M. 2017. Chapter 1 - Introduction. In: Sillanpää, M. and Shestakova, M. eds. *Electrochemical Water Treatment Methods*. Butterworth-Heinemann, 1-46. Available: https://www.sciencedirect.com/science/article/pii/B9780128114629000013 (Accessed

Silverstein, R. M., Webster, F. X. and Kiemle, D. 2005. *Spectrometric Identification of Organic Compounds, 7th Edition*. Wiley.

Singh, A. K. 2020. Microbial Induced Corrosion and Related Theories. In: *Microbially Induced Corrosion and its Mitigation*. Singapore: Springer Singapore, 27-43. Available: https://doi.org/10.1007/978-981-15-8019-2_2 (Accessed

Singleton, R. 2010. Accelerated corrosion testing. *Metal Finishing*, 108 (11): 366-378.

Taheri, N. N., Ramezanzadeh, B. and Mahdavian, M. 2019. Application of layer-by-layer assembled graphene oxide nanosheets/polyaniline/zinc cations for construction of an effective epoxy coating anti-corrosion system. *Journal of Alloys and Compounds*, 800: 532-549.

Taiwo W. Quadri, L. O. O., Omolola E. Fayemi, Moses M. Solomon, and Eno E. Ebenso. 2017. Zinc Oxide Nanocomposites of Selected Polymers: Synthesis, Characterization, and Corrosion Inhibition Studies on Mild Steel in HCl Solution. *ACS Omega*, 5: 8421-8437.

Teodorescu, M. and Bercea, M. 2015. Poly(vinylpyrrolidone) – A Versatile Polymer for Biomedical and Beyond Medical Applications. *Polymer-Plastics Technology and Engineering*, 54 (9): 923-943.

Umoren, S. and Solomon, M. 2014. Recent developments on the Use of Polymers as Corrosion Inhibitors - A Review. *The Open Materials Science Journal*, 8 (1): 39-54.

Umoren, S., Solomon, M. M., Israel, A. U., Eduok, U. M. and Jonah, A. E. 2015. Comparative Study of the Corrosion Inhibition Efficacy of Polypropylene Glycol and Poly (Methacrylic Acid) for Mild Steel in Acid Solution. *Journal of Dispersion Science and Technology*, 36 (12): 1721-1735.

Undavalli, V. K., Ling, C. and Khandelwal, B. 2021. Chapter 6 - Impact of alternative fuels and properties on elastomer compatibility. In: Khandelwal, B. ed. *Aviation Fuels*. Academic Press, 113-132. Available: https://www.sciencedirect.com/science/article/pii/B9780128183144000017 (Accessed

Varney, J., Thompson, N., Moghissi, O., Gould, M. and Payer, J. 2016. *International Measures of Prevention, Application, and Economics of Corrosion Technologies Study*: NACE International: Dublin, Ohio and APQC, Houston, Texas, USA.

Vignal, V., Krawiec, H., Heintz, O. and Oltra, R. 2007. The use of local electrochemical probes and surface analysis methods to study the electrochemical behaviour and pitting corrosion of stainless steels. *Electrochimica Acta*, 52 (15): 4994-5001.

Vivier, V. and Orazem, M. E. 2022. Impedance Analysis of Electrochemical Systems. *Chemical Reviews*, 122 (12): 11131-11168.

Wan, S., Chen, H., Ma, X., Chen, L., Lei, K., Liao, B., Dong, Z. and Guo, X. 2021. Anticorrosive reinforcement of waterborne epoxy coating on Q235 steel using NZ/BNNS nanocomposites. *Progress in Organic Coatings*, 159: 106410.

Wang, X., Li, C., Zhang, M., Lin, D., Yuan, S., Xu, F., Zhou, Y., Wang, C., Zhu, Y. and Wang, H. 2022. A novel waterborne epoxy coating with anti-corrosion performance under harsh oxygen environment. *Chemical Engineering Journal*, 430: 133156.

Xia, S., Zhao, Q., Ji, J., Wu, R., Chen, L., Yin, Y. and Liu, Q. 2023. Impact of Water-Based Coating Substitution on VOCs Emission Characteristics for the Surface-Coating Industries and Policy Effectiveness: A Case Study in Jiangsu Province, China. *Atmosphere*, 14 (4): 662.

Yang, S., Huang, J., Chen, J., Noël, J. J., Barker, I., Henderson, J. D., He, P., Zhang, H., Zhang, H. and Zhu, J. 2022. A Comparative Study on the Anti-Corrosive Performance of Zinc Phosphate in Powder Coatings. *Coatings*, 12 (2): 217.

Yao, H., Li, L., Li, W., Qi, D., Fu, W. and Wang, N. 2022. Application of nanomaterials in waterborne coatings: A review. *Resources Chemicals and Materials*, 1 (2): 184-200.

Zhang, J. and Zhu, A. 2021. Study on the synthesis of PANI/CNT nanocomposite and its anticorrosion mechanism in waterborne coatings. *Progress in Organic Coatings*, 159: 106447.

Zheng Liu, B. Z., Hao Yu,Zhicai Zhang,Wenjuan Jiang and Zengsheng 2022. A Smart Anticorrosive Epoxy Coating Based on Graphene Oxide/Functional Mesoporous Silica Nanoparticles for Controlled Release of Corrosion Inhibitors. *Coatings*, 12 (11): 1749-1755.

APPENDICES

Appendix 1. Classification detailing corrosive atmospheric environments as per ISO 12944-2:2017 standard.

Corrosion class	**Corrosion range**	**Corrosive environments**
C1	Very low	Applies to clean atmospheres, such as offices and schools.
C2	Low	Aimed at low-pollution environments or unheated buildings like warehouses and sports halls.
C3	Medium	Assesses urban and industrial atmospheres with high humidity and some air pollution, such as food breweries, laundries and processing plants.
C4	High	Industrial and coastal areas with moderate salinity, including chemical plants and shipyard.
C5	Very high	Evaluates coastal and maritime areas with high salinity and high pollution.
Cx	Extreme	Extremely corrosive environments like offshore or tropical areas.

Appendix 2. Classification detailing corrosiveness categories for underwater or underground structures as per ISO 12944-2:2017 standard.

Corrosion class	**Corrosive environments**

IM1	Freshwater environments
IM2	Seawater environments
IM3	Underground structures
IM4	Submerged structures with cathodic protection

Appendix 3. ASTM D1654* corrosion resistance rating.

Rating	**Description**	**Corrosion Width (mm)**
10	**No corrosion**	**0 mm**
9	**Trace corrosion**	**≤0.5 mm**
8	**Slight corrosion**	**>0.5 mm to ≤1 mm**
7	**Moderate corrosion**	**>1 mm to ≤2 mm**
6	**Significant corrosion**	**>2 mm to ≤3 mm**
5	**Severe corrosion**	**>3 mm to ≤5 mm**
4–0	**Increasing levels of deterioration**	**>5 mm to complete failure**

* This standard evaluates the degree of corrosion or loss of paint extending from the scribe mark in millimetres (mm) on either side rating of failure at scribe.

Appendix 4. ASTM D3359 - Adhesion Rating.

Classification	Surface of cross-cut areas from which listing has occurred. (Example for six parallel cuts.)	Rate of adhesion
5B	None	The edges of the cuts are completely smooth; none of the squares or the lattice are detached.
4B	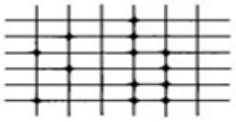	Small flakes of coating are detached at intersections; less than 5% of the area is affected.
3B	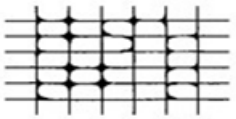	Small flakes of coating are detached along edges and at intersections of cuts. The area affected is 5 to 15% of the lattice.
2B	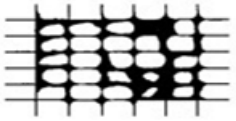	The coating has flaked along the edges and at parts of the squares. The affected area is 15 to 35% of the lattice.
1B	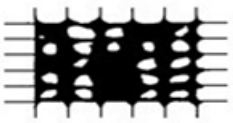	The coating has flaked along the edges of cuts in large ribbons and entire squares have detached. The area affected is 35 to 65% of the lattice.
0B	Flaking and detachment in excess of 65%.	

Appendix 5. ASTM D714 - Blistering Evaluation.

Visual examples illustrating degrees of blistering

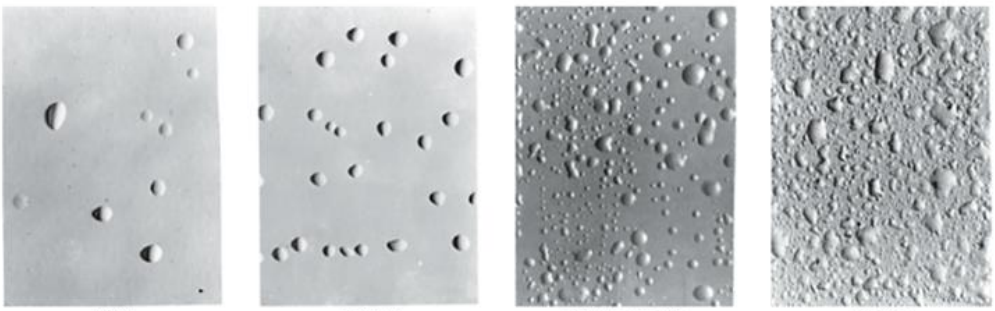

Figure 2 – Blister size #2

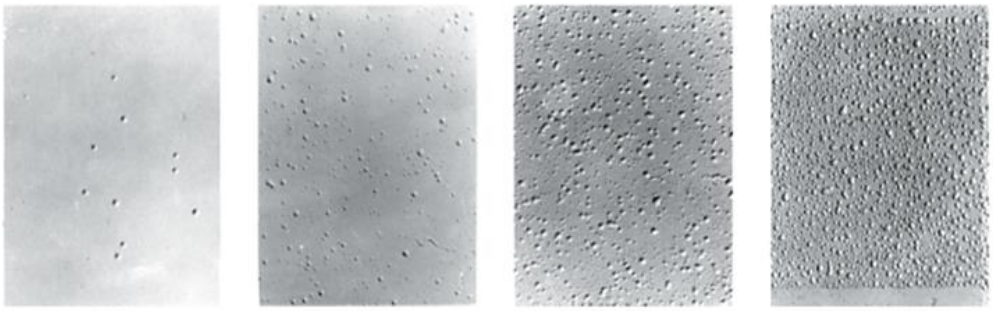

Figure 3 – Blister size #4

Visual examples illustrating degrees of blistering

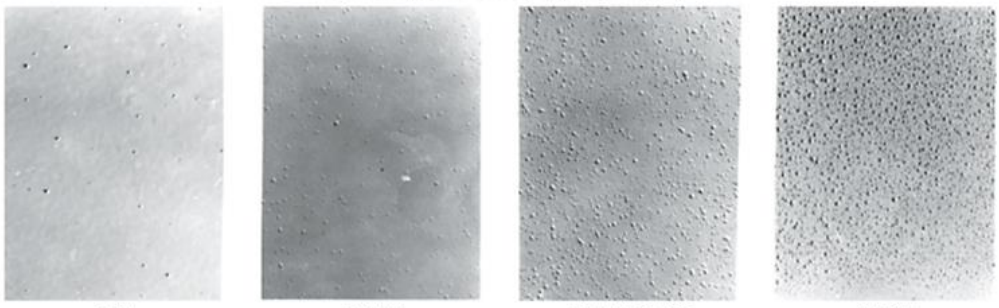

Figure 4 – Blister size #6

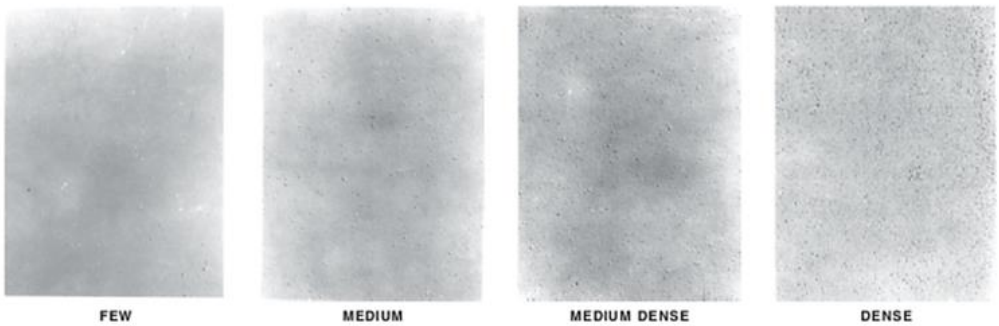

Figure 5 – Blister size #8

Blister Size	Description	Blister Frequency	Description
8	Small blisters	Few (F)	Scattered blisters
6	Moderate-sized blisters	Medium (M)	Moderate blistering over surface
4	Medium-sized blisters	Dense (D)	High density of blisters
2	Large blisters		